Available online at www.sciencedirect.com

SciVerse ScienceDirect

Geochimica et Cosmochimica Acta 85 (2012) 19–40

Geochimica et Cosmochimica Acta

www.elsevier.com/locate/gca

Very high-K KREEP-rich clasts in the impact melt breccia of the lunar meteorite SaU 169: New constraints on the last residue of the Lunar Magma Ocean

Y. Lin [a,*], W. Shen [a], Y. Liu [b], L. Xu [c], B.A. Hofmann [d], Q. Mao [b], G.Q. Tang [b], F. Wu [a], X.H. Li [b]

[a] *Key Laboratory of the Earth's Deep Interior, Institute of Geology and Geophysics, Chinese Academy of Sciences, China*
[b] *State Key Laboratory of Lithospheric Evolution, Institute of Geology and Geophysics, Chinese Academy of Sciences, China*
[c] *National Astronomical Observatories, Chinese Academy of Sciences, China*
[d] *Naturhistorisches Museum der Burgergemeinde Bern, Switzerland*

Received 10 October 2011; accepted in revised form 4 February 2012; available online 21 February 2012

Abstract

In the impact melt breccia (IMB) of Sayh al Uhaymir (SaU) 169, the most KREEP-rich lunar meteorite to date (Gnos et al., 2004), clasts of a new type of lithologies were discovered, consisting of Ca-poor and Ca-rich pyroxenes (60.8 vol.%), Ba-rich K-feldspar (27.9 vol.%), phosphates (5.6 vol.%), Nb-rich ilmenite (4.0 vol.%), zircon (1.2 vol.%) and minor sulfide (0.6 vol.%). These mafic lithic clasts are more enriched in KREEP component (~1500 × CI) than the host meteorite and are highly enriched in potassium. They are referred to as very high-K (VHK) KREEP lithology, and probably most close to the last residual liquid of the Lunar Magma Ocean without significant dilution by other Mg-rich magmas. The fine-grained matrix of the SaU 169 IMB has very similar mineral chemistry to the VHK KREEP lithology, but contains abundant plagioclase with trace K-feldspar. The matrix shows decoupling of K from the REEP-like component; however, it cannot be simply interpreted by mixing the VHK KREEP lithology with anorthosites, which should have diluted the REEP-like component with the same proportion.

SIMS Pb–Pb dating was conducted on zircons in various petrographic settings and with different crystal habits. All analyses show a main age peak at 3921 ± 3 Ma and a smaller one at 4016 ± 6 Ma. The main age peak is identical to the previous Pb–Pb age by Gnos et al. (2006) and U–Pb age by Liu et al. (2009), dating the catastrophic shock event contributed to the formation of SaU 169 IMB. The older ages are consistent with the previous report of an older bulk U–Pb age by Kramers et al. (2007), suggestive of presence of relict crystals in a few large zircon grains. The VHK KREEP clasts predated the fine-grained matrix, but have the same zircon Pb–Pb ages as the latter within the analytical uncertainties. Plagioclase was converted to maskelynite whereas zircon was shocked to diaplectic glass, probably by a second event at ~2.8 Ga. However, the identical zircon Pb–Pb ages of the amorphous parts and the remained crystalline areas indicate no resetting of Pb–Pb isotopes by the later shock metamorphism, or there was another severe impact event postdated solidification of the fine-grained matrix within a few million years.
Crown copyright © 2012 Published by Elsevier Ltd. All rights reserved.

* Corresponding author. Address: Key Laboratory of the Earth's Deep Interior, Institute of Geology and Geophysics, Chinese Academy of Sciences, P.O. Box 9825, 19 Beituchengxi Rd., Beijing 100029, China. Tel.: +86 10 82998413; fax: +86 10 62010846.
E-mail address: linyt@mail.igcas.ac.cn (Y. Lin).

0016-7037/$ - see front matter Crown copyright © 2012 Published by Elsevier Ltd. All rights reserved.
doi:10.1016/j.gca.2012.02.011

1. INTRODUCTION

KREEP is a chemical signature of many Apollo 12 and 14 lunar samples, enriched in potassium (K), rare earth elements (REE), phosphor (P), and other incompatible elements. The similar inter-element ratios of incompatible elements in a wide variety of lunar rocks require a single reservoir of KREEP, which was proposed as the last residual liquid of the postulated Lunar Magma Ocean (LMO) and designated as urKREEP (Warren and Wasson, 1979). However, there are several observations that need clarification. First, various KREEP-rich rocks have high mg# values (atomic ratios of Mg/Mg + Fe), different from the very low mg# predicted by the LMO hypothesis (e.g. mg# 50, Elkins-Tanton et al., 2011). An explanation for this discrepancy is the dilution of urKREEP by high mg# Mg-suite magmas. Second, significant variations in K concentrations are found in many KREEP-rich samples (>0.1 × KREEP) collected from all Apollo sites, which have similar patterns of REEs, P and other incompatible elements (Warren and Wasson, 1979). Since granite is the most K-rich lunar rock (Ryder et al., 1975; Seddio et al., 2010), other high-K KREEP-rich basalts can be explained by partially assimilating granites (Warren et al., 1986; Neal et al., 1989a,b). Alternatively, decoupling of K may be due to silicate liquid immiscibility (SLI) of urKREEP, with K partitioning into the acidic fraction and REEs and P into the mafic fraction (Neal and Taylor, 1988; Jolliff et al., 1999). Finally, a few of exceptionally KREEP-rich clasts (REE > 1000 × CI, e.g. 15405c, 14161 quartz-monzodiorite clasts) were reported in some lunar rocks (Haskin et al., 1973; Jolliff, 1991). These exceptionally KREEP-rich samples usually show differentiated patterns relative to KREEP and probably experienced extended fractional crystallization. Recently, a type of KREEP-rich IMB rock fragments called high-Th KREEP IMB was reported, which is similar to SaU 169 IMB in bulk composition, texture, mineral assemblage and chemistry (Zeigler et al., 2006), and age (Liu et al., 2010).

UrKREEP imposes strict constraints on the LMO hypothesis. However, no pristine urKREEP samples have ever been reported so far. Warren and Wasson (1979) suggested that high-K KREEP-rich rocks were probably the closest approximation of urKREEP, and defined the KREEP component based on the average composition of Apollo-14 breccias with high K, REEs and P. Alternatively, if urKREEP experienced silicate liquid immiscibility and split into K-rich granitic and REEP-rich melts, the chemical composition of the pre-SLI magma can be back-calculated from the lunar glasses that represent known immiscible liquids with K-rich and REEP-rich fractions (Snyder et al., 1991), or from the K-rich granites and the liquid–liquid partition coefficients (Neal and Taylor, 1989).

Sayh al Uhaymir (SaU) 169 is among the most KREEP-rich samples reported up to date, consisting of 87 vol.% of impact melt breccia (IMB) and 13 vol.% of shock-lithified regolith (Gnos et al., 2004). The IMB contains 25–40 vol.% of lithic and mineral clasts in a fine-grained crystalline matrix, highly enriched in incompatible trace elements (ITE) by a factor of ~1.5–1.8 relative to KREEP (using the high-K KREEP composition of Warren and Wasson, 1979, which is used throughout this article to normalize our compositions to), except for K (~0.6 × KREEP). The IMB is a post-shocked melt breccia, and the melting took place after decompression at ambient pressure due to very high post-shock temperatures. This event was dated 3.9 Ga ago by zircon Pb–Pb (Gnos et al., 2004) and zircon U–Pb (Liu et al., 2009). Based on the very high concentrations of U, Th and K and the recorded four impact events, a link of SaU 169 to Imbrium and the location of this meteorite's source region to the Lalande impact crater was suggested (Gnos et al., 2004).

In this work we conducted a comprehensive petrographic, mineral chemistry and SIMS study of the IMB of SaU 169, in order to clarify its precursor rocks. Some of them are expected to contain even higher KREEP components, hence have constraints on petrography and bulk chemistry of the postulated urKREEP melt. SIMS Pb–Pb dating was conducted on zircon with characterized crystal habits and from various petrographic settings, in order to clarify the formation history of the IMB and shock effects on the Pb–Pb isotope system. The preliminary results were reported by Lin et al. (2010).

2. SAMPLE AND EXPERIMENTS

The sample used in this study is a polished thin section of the impact melt breccia of SaU 169, with a total surface area of 0.92 cm^2.

Petrographic observation was conducted with the optical microscope and scanning electron microscope (SEM) type LEO 1500 equipped with an energy dispersive spectrometer (EDS) and a cathodoluminescence (CL) detector. Major and minor elements and REEs of minerals were analyzed using a JEOL JXA-8100 electron probe microanalyzer (EPMA) at the Institute of Geology and Geophysics, Chinese Academy of Sciences, equipped with four wavelength dispersive spectrometers (WDS). The operating conditions were 15 kV accelerating voltage and 20 nA beam current, except that feldspars were analyzed with a slightly defocused beam (~5 μm in diameter) at a current of 10 nA. REE concentrations of zircons and phosphates were quantitatively analyzed by EPMA after the method reported by Zeigler et al. (2008), using a defocused beam with a diameter of 3 μm and a high beam current of 60–120 nA. Each REE was counted for 300–600 s in order to accumulate enough counts. The L_α lines were used for REEs, except that the L_β line was used for Nd. Multi-peak overlapping of individual rare earth elements was corrected for using the overlapping factors that were determined by measuring synthetic single REE phosphate standards. The detection limits of the REEs are 20–70 ppm (except for La of 280–310 ppm). Other standards are natural or synthetic minerals. All raw analyses were corrected for using the traditional ZAF method. The detection limits under normal conditions are (1 SD): 0.01 wt% for K_2O, Na_2O, MgO and Cl, 0.02 wt% for SiO_2, Cr_2O_3, Al_2O_3 and CaO, 0.03 wt% for TiO_2, FeO, MnO and Y_2O_3, 0.04 wt% for BaO and HfO_2, 0.05 wt% for SrO and Ce_2O_3, 0.06 wt% for La_2O_3, 0.09 wt% for Nd_2O_3.

Raman spectra were collected using a Renishaw RM-2000 type laser Raman spectrometer at the Technical Institute of Physics and Chemistry, Chinese Academy of Sciences. The 514.5 nm wavelength of an Ar ion laser was used, with the beam focused on ~1 μm spot of the sample surface. The laser Raman spectrometer was calibrated with a single crystal of silicon standard to the peak at 520.5 cm^{-1}. Raman spectral mapping was conducted on a large zircon grain (30 × 40 μm), scanning from 550 to 1400 cm^{-1} that covers the peak at 1000 cm^{-1} of zircon. The sample stage was moved by a step of 1 μm at both x and y directions during the mapping process.

Zircon Pb–Pb dating was carried out using the CAMECA ims-1280 at the Institute of Geology and Geophysics, Chinese Academy of Sciences. The O_2^- primary beam was used, with a diameter of ~5 μm and a beam current of ~110 pA. Possible isobaric interferences were eliminated at a mass resolution power ($M/\Delta M$, defined at 50% peak height) of ~8000. The combined techniques of oxygen flooding and multi-collector mode were applied as reported by Li et al. (2009). The oxygen flooding technique increases the sensitivity of Pb^+ by a factor of ~2, and significantly decreases anisotropic effects on baddeleyite (Li et al., 2010). $^{204,206,207,208}Pb$ were integrated for 300 s in 50 cycles by electron multipliers (EMs) simultaneously, and the relative efficiency factor of the EM at H1 position (^{207}Pb) was calibrated relative to the central EM (^{206}Pb) using the well-characterized Phalaborwa baddeleyite ($^{207}Pb/^{206}Pb$ = 0.127212). Common Pb was monitored by ^{204}Pb and corrected for using the modern terrestrial value ($^{206}Pb/^{204}Pb$ = 17.8 and $^{207}Pb/^{206}Pb$ = 0.87), assuming that the common Pb is largely surface contamination introduced during sample preparation.

3. RESULTS

3.1. Petrography

Fig. 1 shows the polished thin section of the impact melt breccia (IMB) of SaU 169, and it contains abundant coarse-grained (up to 1.4 mm) mineral clasts of plagioclase (14.1 vol.%), olivine (4.0 vol.%) and low-Ca pyroxene (4.9 vol.%) with a few large grains of kamacite (up to 210 × 560 μm) and merrillite (400 × 700 μm) in a fine-grained (mostly <50 μm) crystalline matrix. In addition, there are seven very high-potassium (VHK) KREEP clasts (1.7 vol.%) and two small basaltic clasts. The total abundance of the clasts is 24.7 vol.%, close to the lower range of the previous estimation (25–40 vol.%, Gnos et al., 2004). The modal abundances of both plagioclase and low-Ca pyroxene clasts were somewhat underestimated because of their grain size continuous variation compared to those in the fine-grained matrix (see details below).

3.1.1. Fine-grained matrix

The fine-grained matrix of the SaU 169 IMB consists predominantly of low-Ca pyroxene (49.8 vol.%) and plagioclase (35.3 vol.%), with less abundant potassium feldspar (5 vol.%), ilmenite (4.3 vol.%), phosphates (4.9 vol.%, merrillite and apatite) and zircon (0.4 vol.%). It has a subophitic texture, with intergrowth of euhedral to subhedral plagioclase and low-Ca pyroxene grains (Fig. 2a). Numerous euhedral grains of plagioclase (mostly <20 μm in width) are enclosed in low-Ca pyroxene, but, the reverse relationship was not found (Fig. 2a). A remarkable feature of plagioclase is the common presence of relict grains. In high-contrast BSE images, sharp boundaries between the relict grains and the overgrown envelops are obvious (Fig. 2b). It was noted that brightness of the relict cores are variable, in comparison with the relatively homogeneous envelops. Minor K-feldspar occurs interstitial to both plagioclase and low-Ca pyroxene, and encloses many small euhedral grains of plagioclase (Fig. 2b and c).

Ilmenite, phosphates and zircon are interstitial to plagioclase and low-Ca pyroxene, and they usually contain small euhedral grains of the latter. Zircon commonly occurs as band-like clusters of crystals, interstitial to plagioclase and low-Ca pyroxene (Fig. 2c). Only a few grains of baddeleyite (<10 μm) were found, enclosed in or coexisting with ilmenite (Fig. 2d).

3.1.2. VHK KREEP clasts

Seven K-feldspar-rich lithic clasts were encountered in the section (Figs. 3–5). The normalized mineral composition of this lithology was calculated from the total surfaces of the componental phases and normalized to 100 vol.%,

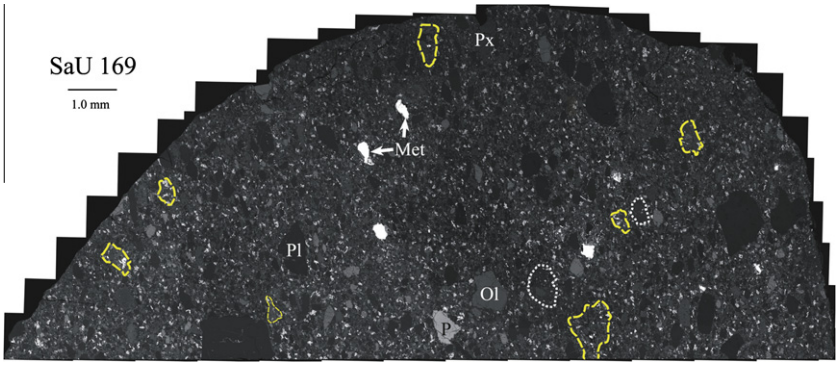

Fig. 1. Photomosaic of back-scattered electron (BSE) images of the impact melt breccia lithology of SaU 169. Abundant clasts of plagioclase (Pl), olivine (Ol) and low-Ca pyroxene (Px), and a few grains of metallic Fe–Ni (Met) and merrillite (P) can be seen. Outlined clasts are VHK KREEP (dashed line) and basalt (dotted line). The scale bar is 1.0 mm.

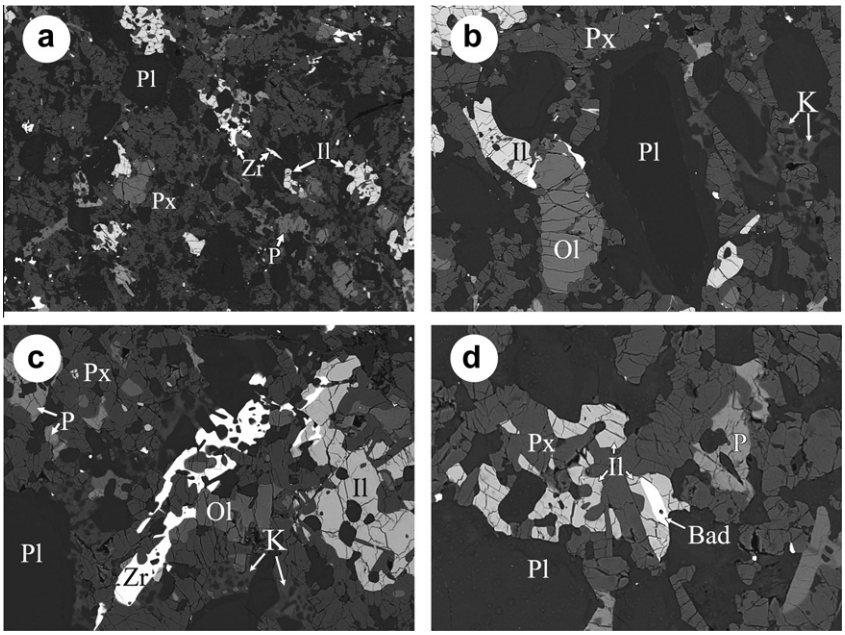

Fig. 2. BSE images of typical textures in the fine-grained matrix of the impact melt breccia lithology. (a) The fine-grained matrix consists mainly of low-Ca pyroxene (Px) and plagioclase (Pl) with less abundant ilmenite (Il), phosphates (P) and minor zircon (Zr). Field of view is 0.67 mm. (b) Plagioclase grains of the matrix commonly have relict cores. Note the sharp and thin boundaries between the cores and margins. The interstitial K-feldspar (K) encloses small euhedral grains of plagioclase. Width of the view is 290 μm. (c) Occurrence of network-like zircon grains in the matrix, interstitial to olivine, pyroxene and plagioclase. There are also small zircon grains coexisting with ilmenite. Width of the view is 245 μm. (d) Occurrence of baddeleyite (Bad) coexisting with ilmenite in the matrix. Width of the view is 170 μm.

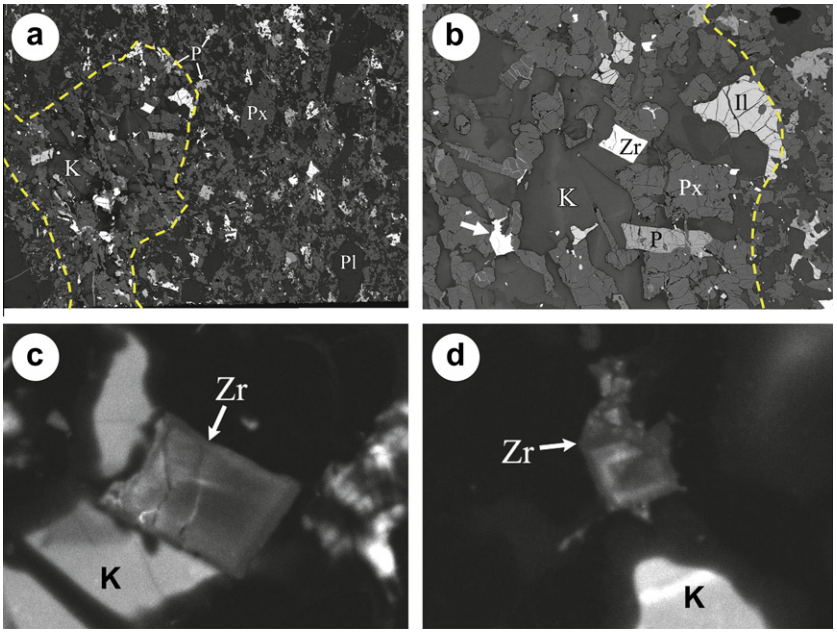

Fig. 3. VHK KREEP clast #1. (a) BSE image of the VHK KREEP clast, consisting mainly of K-feldspar and pyroxenes (Ca-rich and Ca-poor pyroxenes cannot be distinguished here) with less abundant ilmenite, phosphates and zircon. The presence of abundant K-feldspar is typical of the VHK KREEP clast. Also note the coarser-grained texture of the clast in comparison with the surrounding matrix. Dashed lines show the boundaries of the clast. Width of the view is 0.83 mm. (b) Close-up image of two zircon grains in the clast. Note cracks in the VHK-KREEP zircon grains and heterogeneity of K-feldspar. Dashed lines show the boundaries of the clast. Note the jump in grain size at the clast–matrix boundary. Width of the view is 245 μm. (c) Cathodoluminescence (CL) image of the larger zircon grain in (b), showing CL zoning and bright CL of K-feldspar. Width of the view is 110 μm. (d) CL image of the smaller zircon grain (labeled as arrow) in (b), showing the zoning and fine clast-like texture of zircon. Width of the view is 110 μm. Abbreviations as in Fig. 2.

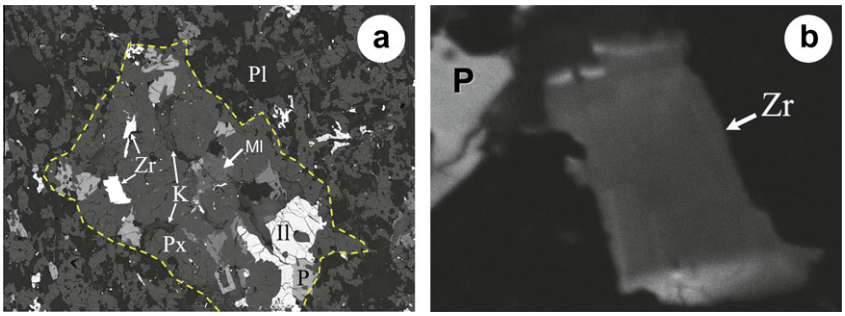

Fig. 4. VHK KREEP clast #2. (a) BSE image of the clast, consisting predominantly of coarse-grained pyroxenes with less abundant K-feldspar, ilmenite, phosphates and zircon. Note shock-induced melting (Ml) in the center of the clast. Dashed lines show the boundaries of the clast. Width of the view is 720 μm. (b) CL image of the largest zircon grain in the clast, showing a zoning texture. Width of the view is 80 μm. Abbreviations as in Fig. 2.

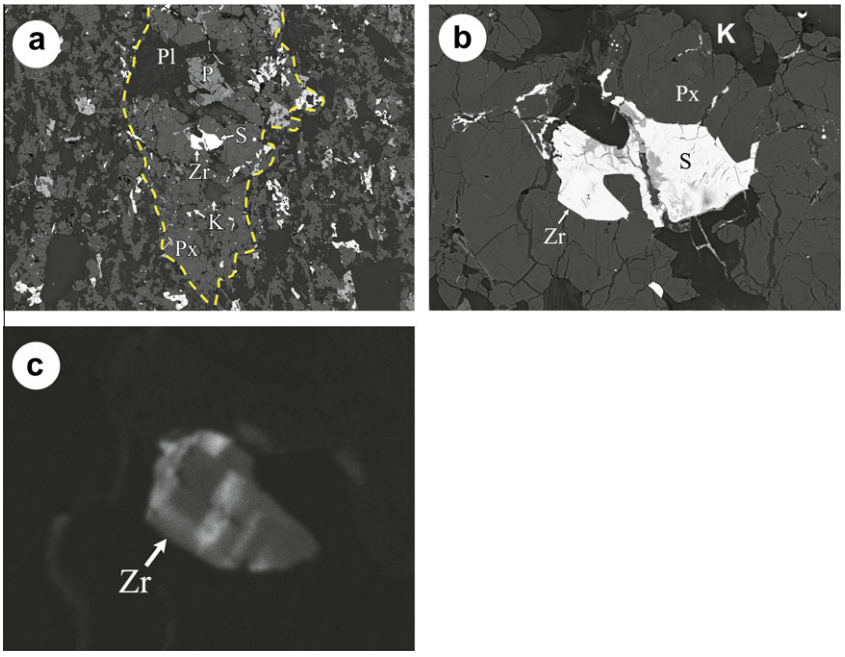

Fig. 5. VHK KREEP clast #3. (a) BSE image of the clast in the middle, consisting of coarse-grained pyroxenes and K-feldspar with minor phosphates, ilmenite and zircon. The large zircon grain coexists with sulfide (S). Dashed lines show the boundaries of the clast. Width of the view is 0.99 mm. (b) Close-up image of the large zircon coexisting with sulfide, note fractures of the zircon. Width of the view is 170 μm. (c) CL image of the large zircon grain, showing a zoning texture. Width of the view is 70 μm. Other abbreviations are the same as in Fig. 2.

consisting of 60.8 vol.% pyroxenes, 27.9 vol.% K-feldspar, 4.6 vol.% merrillite, 1.0 vol.% apatite, 4.0 vol.% ilmenite, 1.2 vol.% zircon and 0.6 vol.% sulfide. These lithic clasts are, hereafter, referred to as VHK KREEP clasts, based on their very high concentrations of K, REEs and P (indicated by the high abundances of K-feldspar, zircon and phosphates).

From the VHK KREEP clasts to the fine-grained matrix, variation in the mineral assemblages and textures is evident, although no sharp boundaries between both lithologies is optically discernable or at high BSE contrast. First, the VHK KREEP clasts are unique through presence of K-feldspar as a major constituent, whereas the fine-grained matrix is plagioclase-rich with only a trace K-feldspar. In addition, the scattered grains of K-feldspar in the fine-grained matrix are typical with small euhedral inclusions of plagioclase as described above and shown in Fig. 2b and c. This is different from the large grains in the VHK KREEP clasts (Figs. 3a, b, 4a and 5a). Second, Ca-rich pyroxene is abundant in the VHK KREEP, but few grains were found in the fine-grained matrix. Third, the VHK KREEP clasts are coarse-grained compared to the fine-grained matrix. This is evident for pyroxene as shown in Fig. 4a, with the coarse grains in the VHK KREEP clasts compared to the small grains intergrown with plagioclase in the matrix. The few largest zircon grains (up to 30 × 40 μm) are also located within the VHK KREEP clasts, whereas those in the matrix usually occur as clusters of

small crystallites (Fig. 2a and c). The large zircon grains have usually fractures (Figs. 3b, 4a and 5b) and show concentric or sector zoning of CL (Figs. 3c, d, 4b and 5c).

3.1.3. Basaltic and anorthositic clasts

Two basaltic clasts (300×450 μm, 460×800 μm, respectively) were found in the section. They show subophitic texture and consist predominantly of plagioclase and low-Ca pyroxene with trace ilmenite and phosphates (Fig. 6a). The grain size (mostly <10 μm width) of the basaltic clasts is distinctly smaller than the fine-grained matrix.

Fig. 6b shows an anorthositic clast predominantly consisting of heterogeneous plagioclase with minor amounts of small ilmenite and phosphate grains.

3.1.4. Mineral clasts

Clasts of various minerals are abundant in the section. Relative to the homogeneous grains of the fine-grained matrix, low-Ca pyroxene clasts commonly show normal zoning and exhibit darker cores in BSE images (Fig. 7a). The rims of the pyroxene clasts are continuous to the host matrix, probably resorbed by and intergrown with the latter. Plagioclase clasts are very abundant and readily recognizable through presence of the overgrown rims on the irregular cores. The plagioclase clast grain sizes vary from tens micrometers, as small as those in the fine-grained matrix, up to 1.4 mm. The large plagioclase clasts usually contain numerous cracked inclusions (Fig. 7b) that appear darker in CL images (Fig. 7c). Under high magnification, the dark

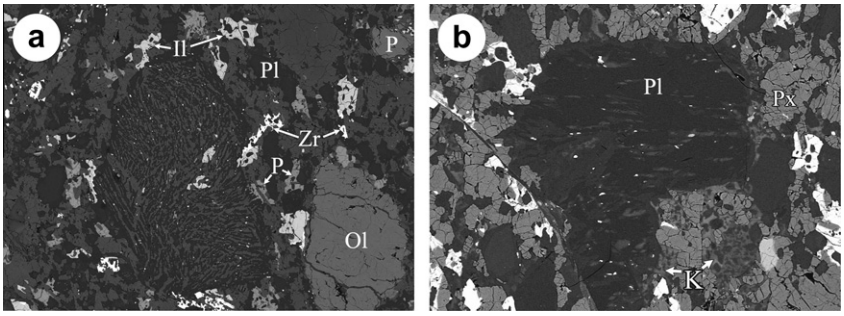

Fig. 6. BSE images of other lithic clasts. (a) A basaltic clast in the center of view, consisting of fine-grained low-Ca pyroxene (gray) and plagioclase (dark gray) with trace ilmenite (light gray) and phosphates (not visible). Width of image is 850 μm. (b) An anorthositic clast, consisting predominant grains of plagioclase with tiny ilmenite and phosphates. Note heterogeneity of the plagioclase assemblage and a thin shear vein at the left side. Width of the view is 390 μm. Abbreviations are the same as in Fig. 2.

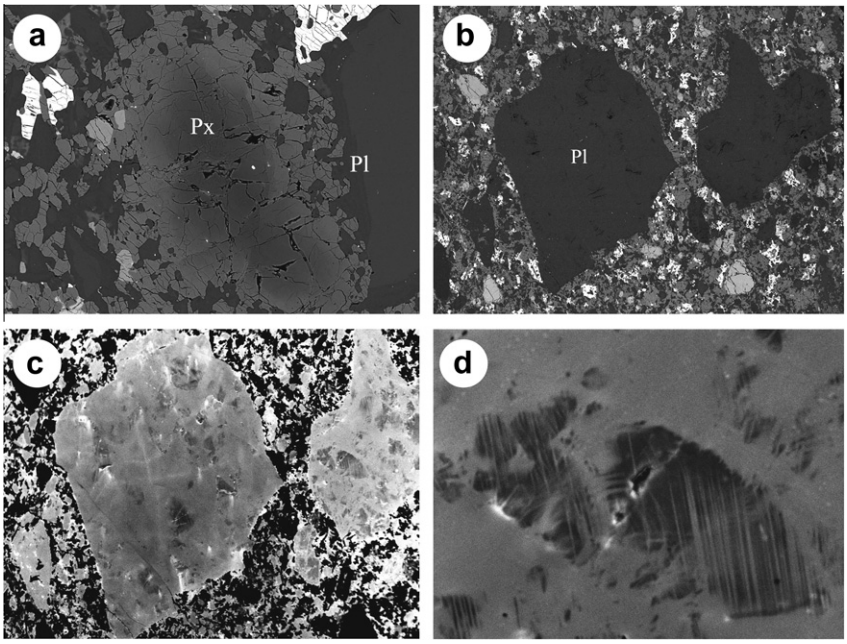

Fig. 7. BSE images of mineral clasts. (a) A normally zoned low-Ca pyroxene clast, intergrown with plagioclase at its margin and showing gradational contact to the fine-grained matrix. On the right side is a plagioclase clast with dark rim. Width of the view is 320 μm. (b) Two large plagioclase clasts containing abundant fractures. Width of the view is 2.3 mm. (c) CL image of the plagioclase clasts in (b), showing dark CL of the fractured inclusions, and dense and thin lamellae. Width of the view is 1.7 mm. (d) Close-up CL image of a fractured inclusions, showing a lamellae texture. Width of the view is 240 μm. Abbreviations are the same as in Fig. 2.

inclusions show lamella textures in the CL images (Fig. 7d). The overgrown rims of plagioclase are rarely found on the largest clasts, but are common on smaller ones.

Majority of olivine occurs as crystal clasts up to 0.84 mm in size (Fig. 1). They appear homogeneous. A large clast of merrillite (400 × 700 μm, Fig. 1) was also found in the section without any silicate inclusions. This is in contrast to most interstitial phosphates in the fine-grained matrix. There are no grains of apatite coexisting with this large merrillite clast. Metallic Fe–Ni clasts (up to 210 × 560 μm) are common in the section (Fig. 1), coexisting with phosphates and sulfide. Small rounded grains of metal and sulfide are surrounding metal clasts.

3.2. Shock features

3.2.1. Melt pockets and veinlets

There are several shock-induced melt pockets with numerous droplets of metallic Fe–Ni and sulfide (Fig. 8a), indicative of melting. Partially melted plagioclase grains occur as flow-structured stripe within the melt pockets. Most of the melt pockets contain abundant vesicles with size significantly decreasing towards their margins (Fig. 8b). There are a few of impact melt veinlets that only contain small amount of melt in their matrix (Fig. 8c).

3.2.2. Phase transformation

Plagioclase is isotropic under cross polarized light, indicative of diaplectic glass (maskelynite). This is confirmed by their Raman spectra (Fig. 9a). In comparison with low-Ca pyroxene that is usually fractured, the surface of plagioclase is very smooth (e.g. Fig. 2). Only large plagioclase clasts have fractured inclusions (e.g. Fig. 7b). Raman spectra of these fractured inclusions confirmed the crystalline state of plagioclase (Fig. 9a). In addition, the fractured inclusions can also be distinguished from the smooth surface in CL images (Fig. 7c and d).

Similar to plagioclase, most grains of zircon have smooth surfaces. Only a few of the largest zircon grains have fractures (e.g. Fig. 3b). Laser Raman analysis of zircon revealed that the smooth areas have been transformed to amorphous phase (Fig. 9b), whereas the fractured areas retain vibrational Raman bands of zircon. Fig. 9c shows Raman spectra of the large zircon grain in Fig. 3b, plotted with the intensity of the peak at ~1000 cm^{-1}. It is obvious that the fractured part remained crystalline, whereas the smooth area has been transformed to amorphous phase.

3.3. Mineral chemistry

3.3.1. Olivine

Most olivine clasts have homogeneous compositions, with the Fo contents of 58–62 mol% and MnO contents of 0.24–0.40 wt%. No fayalite grains were found in the section. The largest clast has distinctly higher Fo contents (63–68 mol%), but with the same MnO content (0.24–0.35 wt%). The CaO concentrations vary from 0.06 to 0.28 wt%, with exception of two grains (0.38 and 0.43 wt%). The representative analyses are given in Table 1.

3.3.2. Pyroxenes

The low-Ca pyroxenes in the fine-grained matrix, VHK KREEP clasts and basalt clasts have almost identical and relatively homogeneous compositions (Figs. 10 and 11).

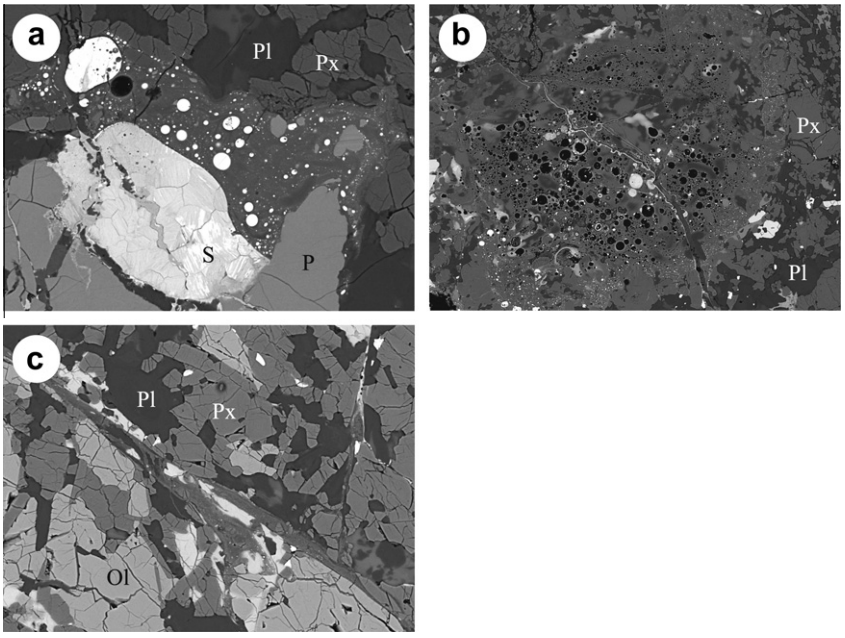

Fig. 8. BSE images of melt pockets and veinlets. (a) A melt pocket in a sulfide-rich area, with numerous sulfide droplets. Plagioclase occurs as dark curved stripes, and the melt shows no evidence of re-crystallization. Below the melt pocket there is a heavily weathered sulfide (S) assemblage. Width of the view is 125 μm. (b) Another melt pocket with abundant vesicles (dark), with the diameters of the vesicles decreasing outwards. Width of the view is 470 μm. (c) Two thin shock-induced melt veinlets consisting of relict clasts and very fine-grained matrix. Width of the view is 160 μm. Abbreviations are the same as in Fig. 2.

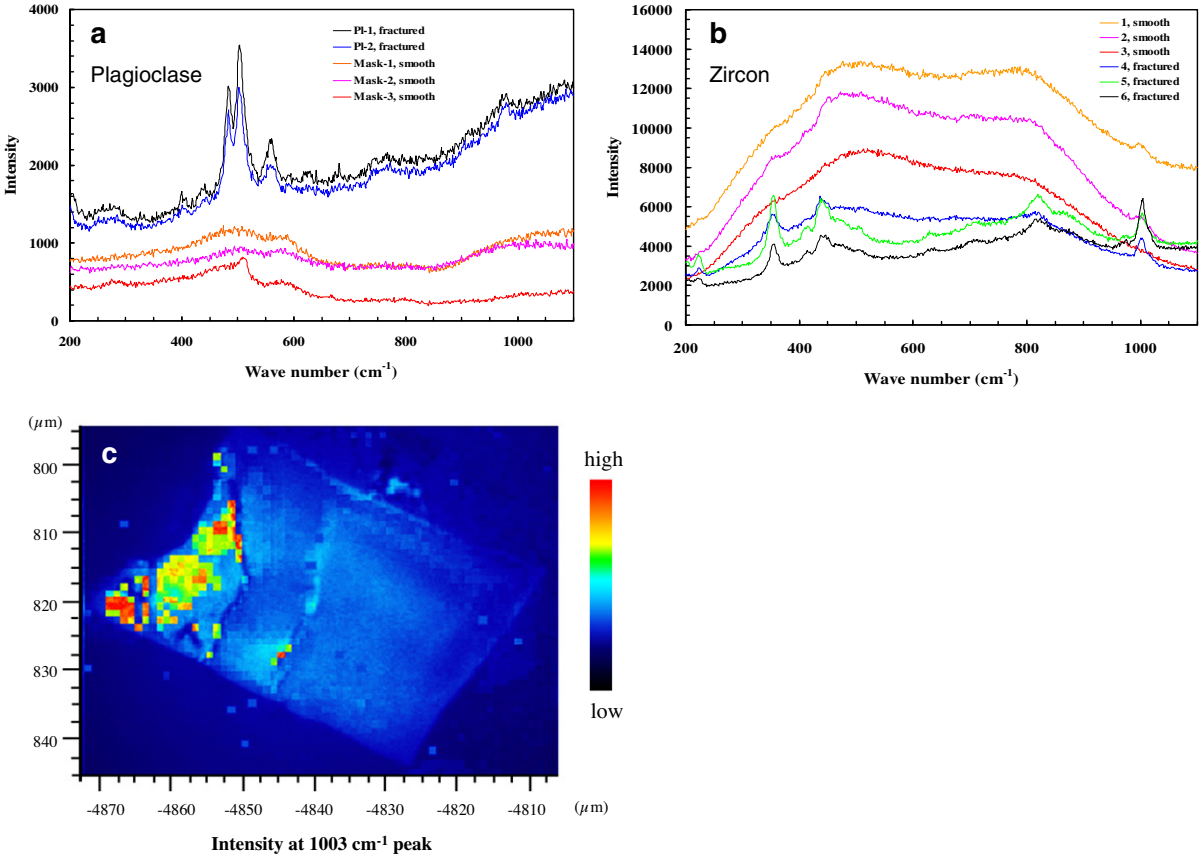

Fig. 9. Raman spectra of minerals. (a) Maskelynite (Mask) and relict plagioclase (Pl); (b) fractured and smooth surfaces of zircon, the characteristic Raman peaks remain in the former but disappear in the latter; (c) the intensity at 1003 cm^{-1} band of Raman spectra of the large zircon grain shown in Fig. 3b and c. Note the similar spatial distribution of the peak intensity with the fractured areas.

In contrast, the clasts of low-Ca pyroxene display a significantly wider range of Fs contents (15–36 mol%) than the other occurrences (27–35 mol%) (Fig. 10). Plots of FeO vs CaO, MnO, Cr_2O_3, and TiO_2 vs Cr_2O_3 confirm the differences between the clasts and other occurrences (Fig. 11).

Ca-rich pyroxene was found mainly in the VHK KREEP clasts, coexisting with low-Ca pyroxene. It has a relative narrow range of compositions ($Fs_{16–19}Wo_{36–43}En_{42–46}$, except for two analyses of $Fs_{22,24}Wo_{29,26}En_{49,50}$), in equilibrium with the low-Ca pyroxene at ~1000 °C (Fig. 10). Other minor elements are Al_2O_3 (1.01–2.18 wt%), TiO_2 (0.72–1.67 wt%), Cr_2O_3 (0.15–0.47 wt%), MnO (0.16–0.32 wt%) and Na_2O (0.10–0.23 wt%).

3.3.3. Feldspars

The coarse-grained plagioclase clasts are homogeneous, without significant zoning. Analyses of the fractured inclusions of the large plagioclase clasts reveal no recognizable differences from the surrounding smooth host (Table 2). However, a large compositional variation ($An_{57–90}Ab_{10–39}Or_{<4}$) was found among the clasts (Fig. 12). Furthermore, this compositional heterogeneity is also seen in the relict cores of plagioclase. In contrast, the overgrown margins of plagioclase have a relatively narrow compositional range ($An_{73–84}Ab_{15–26}Or_{<1.3}$) in comparison with their relict cores ($An_{69–94}Ab_{6–30}Or_{<1.4}$). The FeO concentrations seem to be slightly higher in the grains of the fine-grained matrix than the large plagioclase clasts (Table 2).

K-feldspar shows large compositional variation among the clasts and even in individual grains. It is characterized by BaO-enrichment (1.15–5.62 wt%, see Fig. 12b). Ba substitutes for K, and has no inverse correlation with Na. FeO concentrations are less than 0.42 wt%.

3.3.4. Phosphates

REE-enrichment is typical of lunar merrillite grains, up to 1.17 wt% La_2O_3, 2.84 wt% Ce_2O_3, 1.48 wt% Nd_2O_3 and 2.79 wt% Y_2O_3 (Table 3). It is also named as RE-merrillite (Jolliff et al., 2006). The REE contents of merrillite have relatively narrow variation ranges (by factors of 1.4–2.0), except for distinctly lower REE contents of several grains coexisting with the kamacite clasts (Fig. 13). The compositions of the grains in the VHK KREEP clasts and the fine-grained matrix are indistinguishable. The large merrillite clast has similar REE contents of the VHK KREEP clasts and the fine-grained matrix, but closer to their lower limits (Fig. 13). Other minor elements are MgO (3.17–3.77 wt%), Na_2O (0.40–0.84 wt%) and FeO (0.72–2.21 wt%). The REE-poor grains coexisting with the metals contain higher Na_2O contents (1.18–1.27 wt%).

Table 1
Representative compositions of olivine and pyroxenes, in wt%.

	Olivine					Low-Ca pyroxene							Ca-pyroxene	
	Clast			Matrix		KREEP		Clast			Matrix		VHK KREEP	
	1	2	3	4	5	6	7	8[a]	9[b]	10	11	12	13	14
SiO_2	36.6	36.3	36.5	35.7	36.3	53.2	53.1	55.3	52.0	53.0	52.2	52.4	52.0	51.9
TiO_2	0.06	0.04	0.04	0.15	b.d.	0.44	0.72	0.41	0.71	0.88	0.65	0.72	0.78	0.72
Al_2O_3	0.06	0.05	b.d.	0.12	0.03	0.67	0.77	1.11	1.11	0.61	0.92	1.18	1.27	1.01
Cr_2O_3	0.07	0.06	0.05	0.07	b.d.	0.15	0.21	0.38	0.28	0.27	0.23	0.33	0.29	0.24
FeO	28.8	34.6	33.6	35.2	35.0	19.8	20.5	10.0	20.2	19.3	20.8	19.8	9.67	10.0
MnO	0.26	0.36	0.29	0.37	0.30	0.30	0.35	0.12	0.25	0.27	0.39	0.26	0.18	0.21
MgO	33.8	29.2	30.0	28.0	28.8	22.3	22.5	31.3	22.2	24.0	22.4	23.1	14.8	14.8
CaO	0.14	0.12	0.15	0.27	0.14	2.68	2.07	0.94	1.94	1.28	2.11	1.92	19.4	20.0
Na_2O	b.d.	0.01	b.d.	0.01	0.03	0.01	b.d.	0.01	b.d.	b.d.	b.d.	0.04	0.19	0.15
Total	99.7	100.7	100.7	99.8	100.5	99.5	100.3	99.5	98.7	99.6	99.7	99.7	98.6	99.0
Cations per formular unit														
Si	0.987	0.997	0.998	0.993	0.999	1.979	1.966	1.954	1.955	1.961	1.950	1.945	1.963	1.958
Ti	0.001	0.001	0.001	0.003	0.000	0.012	0.020	0.011	0.020	0.024	0.018	0.020	0.022	0.020
Al	0.002	0.002	0.000	0.004	0.001	0.029	0.034	0.046	0.049	0.027	0.040	0.052	0.057	0.045
Cr	0.002	0.001	0.001	0.002	0.000	0.004	0.006	0.011	0.008	0.008	0.007	0.010	0.009	0.007
Fe	0.650	0.794	0.768	0.821	0.806	0.616	0.635	0.295	0.635	0.597	0.648	0.613	0.305	0.315
Mn	0.006	0.008	0.007	0.009	0.007	0.009	0.011	0.003	0.008	0.009	0.012	0.008	0.006	0.007
Mg	1.358	1.194	1.222	1.161	1.182	1.233	1.241	1.650	1.244	1.321	1.248	1.278	0.831	0.831
Ca	0.004	0.003	0.004	0.008	0.004	0.107	0.082	0.035	0.078	0.051	0.084	0.076	0.783	0.806
Na	0.000	0.001	0.000	0.000	0.001	0.001	0.000	0.001	0.000	0.000	0.000	0.003	0.014	0.011
Fo/En	67.6	60.0	61.4	58.6	59.5	63.0	63.4	83.3	63.6	67.1	63.0	65.0	43.3	42.5
Wo						5.4	4.2	1.8	4.0	2.6	4.3	3.9	40.8	41.3

b.d., below detection.
[a] Core.
[b] Rim.

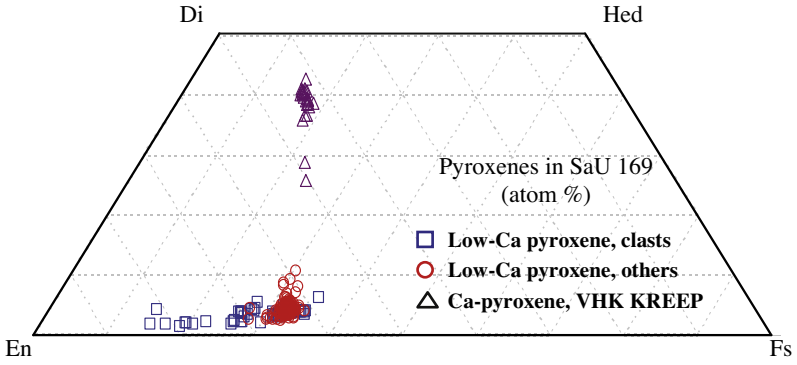

Fig. 10. Quadrilateral diagram of pyroxenes with various occurrences. Note a wider range of the low-Ca pyroxene clasts, in comparison with those in the matrix and the VHK KREEP clasts (others).

In comparison with merrillite, apatite has significantly lower contents of REEs (Table 3 and Fig. 13). In addition, the apatite grains in the VHK KREEP clasts appear to contain more REEs and less FeO than those in the fine-grained matrix (Fig. 13). The other minor elements in apatite are Cl (0.80–1.54 wt%), F (2.36–3.09 wt%), FeO (0.26–2.39 wt%) and SiO_2 (0.33–0.80 wt%).

Ce_2O_3/Y_2O_3 ratios of merrillite slightly increase from 0.86 to 1.08 with the Ce_2O_3 contents. In contrast, apatite displays a wide range of Ce_2O_3/Y_2O_3 ratios (0.5–2.5) with relatively narrow and low Ce_2O_3 contents. However, large analytical errors are expected in the apatite REE-results because of much lower REE contents in apatite than in merrillite. Fig. 14 shows CI/normalized REE patterns of merrillite and apatite achieved by long EPMA counting. Merrillite shows LREE-rich patterns with negative Eu anomaly, decreasing from La $\sim 10^4 \times$ CI to Y $\sim 5 \times 10^3 \times$ CI. The REE patterns of apatite are nearly parallel to those of merrillite, but lower by a factor of $\sim$8 in abundance, with Ce $\sim 1.6 \times 10^3 \times$ CI and Y $\sim 4 \times 10^2 \times$ CI.

3.3.5. Zircon and baddeleyite

Zircons in the VHK KREEP clasts and the fine-grained matrix have nearly identical compositions (Fig. 15), with relatively homogeneous HfO_2 (1.14–1.53 wt%) but variable Y_2O_3 (<1.35 wt%). There seems to be a weak correlation

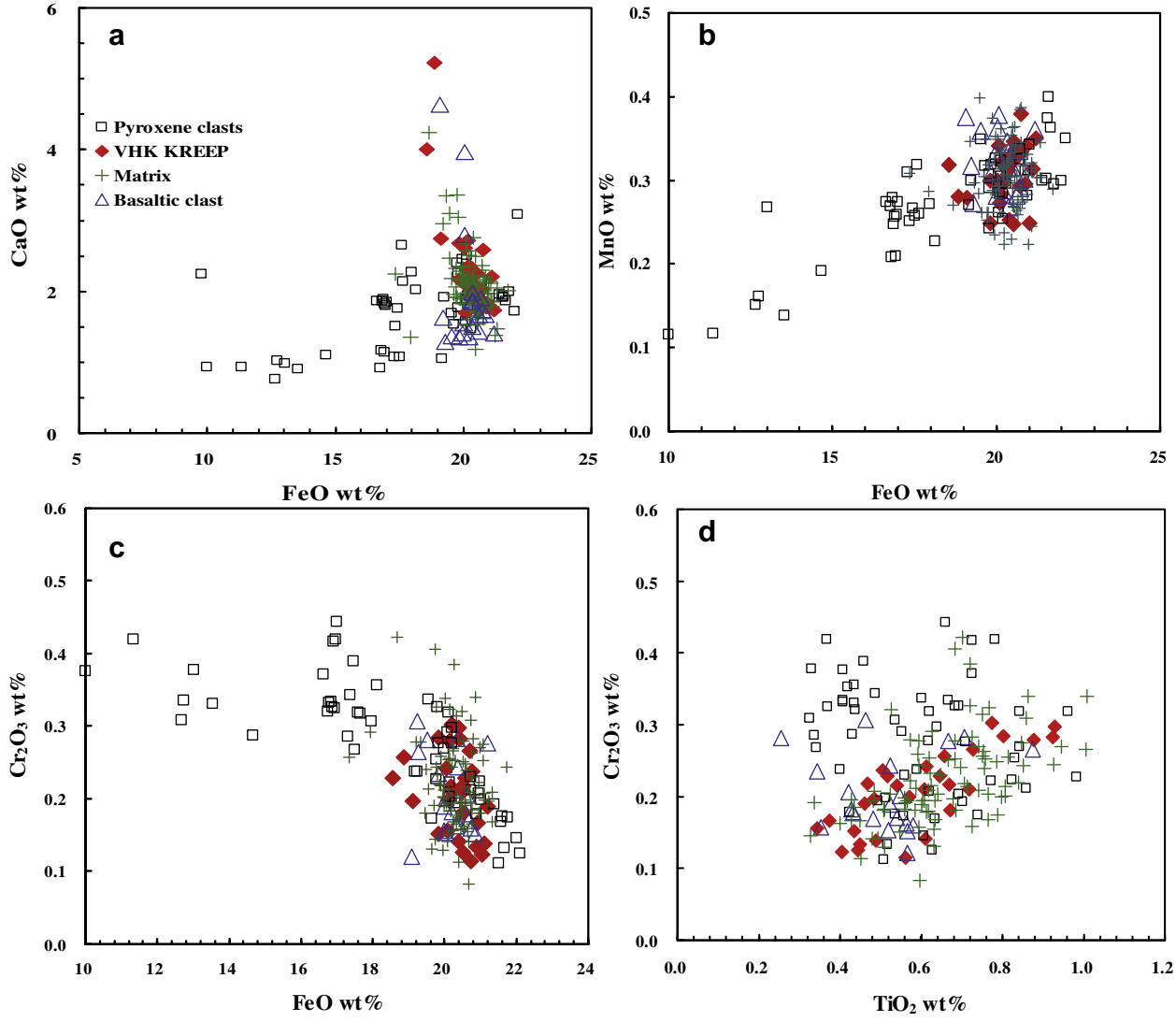

Fig. 11. Compositional diagrams of low-Ca pyroxene from various occurrences. The pyroxene clasts display wider compositional range than those in the matrix, VHK KREEP clasts and basaltic clasts.

between minor FeO (<1.09 wt%) and Na_2O (<0.75 wt%). A few zircon grains enclosed in ilmenite contain the lowest Y_2O_3 (<0.14 wt%) but higher HfO_2 (1.35–2.15 wt%) and FeO (1.04–1.85 wt%). The Na_2O-content is within the range of other occurrences. The long-time counting EPMA analysis reveals HREE-rich and Eu negative anomaly patterns of zircon (Fig. 14), increasing from Ce ~290 × CI to Yb ~10^4 × CI.

Only a few grains of baddeleyite were encountered and were analyzed (Table 4). They are HfO_2-rich (2.36–3.22 wt%), and contain minor Nb_2O_5 (0.62–0.83 wt%), Ta_2O_5 (<0.16 wt%), LREEs (La_2O_3 < 0.11 wt%, Ce_2O_3 < 0.13 wt%), FeO (1.18–1.56 wt%), TiO_2 (1.20–3.14 wt%), SiO_2 (<0.51 wt%) and CaO (<0.69 wt%).

3.4. Pb–Pb dating

All 42 analyses of Pb–Pb isotopic ratios and inferred ages conducted on 16 zircon grains and one grain of baddeleyite are listed in Table 5. Correction for common lead is relatively small, as indicated by the low $^{204}Pb/^{206}Pb$ ratios of 2×10^{-3}–1×10^{-5}.

As described above, a few large zircon grains (e.g. Fig. 3b and c) have cracks where the zircon remains crystalline as indicated by Raman spectra (e.g. Fig. 9a and c). Eight Pb–Pb analyses of these fractured areas on five zircon grains in the VHK KREEP clasts have Pb–Pb ages from 3893 to 4049 Ma with a major peak at 3922 ± 7 Ma, undistinguishable from those of the smooth areas (3885–4006 Ma, with a peak at 3915 ± 5 Ma). On the other hand, the large zircon grains often depict CL zoning (Figs. 3c, d, 4b and 5c), and some of them look like fine clasts embedded in dark matrix (Fig. 3d). Additional efforts were taken to investigate any possible correlation between the Pb–Pb ages and CL zoning of zircon. After SIMS analysis, the section was studied at BSE-SEM to check precise positions of the ion sputtered pits. However, no significant relationship between the CL zoning and Pb–Pb ages was found, probably

Table 2
Representative analyses of feldspars, in wt%.

	Plagioclase										Orthoclase			
	Clast				Matrix						VHKKREEP			
	1[a]	2[a]	3[b]	4[b]	5[c]	6[d]	7[c]	8[d]	9[c]	10[d]	11	12	13	14
SiO_2	48.5	47.7	47.9	48.5	50.8	48.2	48.6	48.6	45.0	47.0	65.1	61.6	62.6	59.9
Al_2O_3	33.3	33.7	33.4	33	31.2	34.1	33.3	33.0	36.0	33.7	18.6	19.5	20.4	20.7
FeO	0.23	0.38	0.14	0.24	0.25	0.33	0.42	0.34	0.38	0.31	0.16	0.33	0.08	0.11
BaO	0.12	b.d.	0.11	b.d.	0.11	b.d.	b.d.	0.04	0.05	b.d.	1.22	3.33	4.10	5.62
CaO	16.2	16.5	16.4	16.4	14.2	16.8	16.1	15.6	18.9	16.9	0.16	0.25	0.72	0.93
SrO	0.07	b.d.	0.06	0.05	0.10	0.08	b.d.	0.10	b.d.	b.d.	0.10	0.08	0.09	0.17
Na_2O	2.25	1.92	1.80	2.19	3.41	1.84	2.27	2.53	0.70	1.70	1.24	0.81	1.35	0.93
K_2O	0.21	0.17	0.18	0.21	0.25	0.12	0.14	0.09	0.02	0.06	13.6	13.3	12.5	11.6
Total	100.9	100.4	100.0	100.7	100.5	101.4	101.0	100.3	101.1	99.8	100.2	99.2	101.9	100.0
Cations per formular unit														
Si	2.206	2.182	2.195	2.211	2.310	2.179	2.210	2.219	2.057	2.165	2.994	2.918	2.894	2.852
Al	1.784	1.814	1.803	1.773	1.673	1.818	1.782	1.777	1.942	1.828	1.011	1.089	1.112	1.160
Fe	0.009	0.015	0.005	0.009	0.009	0.012	0.016	0.013	0.014	0.012	0.006	0.013	0.003	0.005
Ba	0.002	0.000	0.002	0	0.002	0.000	0.000	0.001	0.001	0.000	0.022	0.062	0.074	0.105
Ca	0.789	0.806	0.806	0.801	0.693	0.813	0.782	0.764	0.925	0.835	0.008	0.013	0.035	0.047
Sr	0.002	0.001	0.002	0.001	0.003	0.002	0.001	0.003	0.000	0.000	0.003	0.002	0.002	0.005
Na	0.198	0.170	0.160	0.193	0.301	0.161	0.200	0.224	0.062	0.152	0.111	0.075	0.121	0.086
K	0.012	0.010	0.011	0.012	0.015	0.007	0.008	0.005	0.001	0.004	0.797	0.801	0.738	0.701
An	79.0	81.7	82.5	79.6	68.7	82.9	79.0	76.9	93.6	84.3	0.9	1.3	3.7	5.0
Ab	19.8	17.3	16.4	19.2	29.8	16.4	20.2	22.6	6.3	15.3	11.8	7.9	12.5	9.2
Or	1.2	1.0	1.1	1.2	1.4	0.7	0.8	0.5	0.1	0.4	85.0	84.3	76.2	74.6
Cls	0.2	0.0	0.2	0	0.2	0.0	0.0	0.1	0.1	0.0	2.3	6.5	7.7	11.2

b.d., below detection; An, anorthite; Ab, albite; Or, orthoclase; Cls, Celsian.
[a] Smooth.
[b] Fractured.
[c] Core.
[d] Rim.

due to the small grain sizes and/or their similar ages relative to the analytical uncertainty.

Fig. 16 shows a histogram of all 42 Pb–Pb ages, with an age dichotomy at 3921 ± 3 (2σ) Ma and 4016 ± 6 (2σ) Ma, respectively. Most of the analyses (81%) belong to the main peak at 3921 Ma, and there are eight analyses that could be assigned to 3980–4050 Ma. The difference between both age peaks is 85 Ma, significantly larger than the analytical uncertainty at 95% confidence level. The Pb–Pb age of baddeleyite is 3935 ± 17 (2σ) Ma, plots within the main peak. Statistical analysis of the Pb–Pb ages of zircon in the VHK KREEP clasts (3918 ± 9, 4011 ± 29 Ma) and the fine-grained matrix (3923 ± 7, 4023 ± 59 Ma) reveals no distinguishable difference between them.

4. DISCUSSION

4.1. Lithic clasts of the VHK KREEP lithology

As described in Section 3.1, the VHK KREEP assemblages are referred to as clasts, because they are texturally well-defined lithic relicts instead of being K-feldspar-enriched areas of the fine-grained matrix that crystallized from a post shock melt. Evidence for an exotic origin of the VHK KREEP clasts includes: (1) the occurrence and abundance of K-feldspar in the VHK KREEP clasts are distinct from those in the fine-grained matrix. In the VHK KREEP clasts, K-feldspar is the major component (27.9 vol.%) with only minor plagioclase. In contrast, plagioclase is the major mineral in the matrix, with minor and interstitial K-feldspar. Furthermore, K-feldspar appears significantly larger, free of plagioclase inclusions, in the VHK KREEP clasts (e.g. Fig. 3a) than those in the matrix, which contain abundant euhedral inclusions of plagioclase (e.g. Fig. 2b). (2) The coarse-grained texture of the VHK KREEP clasts is unambiguously different from the fine-grained texture of the matrix. Besides K-feldspar described above, pyroxene is also significantly larger in size in the VHK KREEP clasts (e.g. Fig. 4a) than grains in the matrix. In addition, zircon appears as larger individual grains without plagioclase inclusions in the VHK KREEP clasts (e.g. Figs. 3b and 4a), in comparison to the fine-grained clusters in the matrix (e.g. Fig. 2c). All these crucial petrographic details were not recognized before.

Although there are no apparent sharp spatial boundaries between the VHK KREEP clasts and the matrix, the abrupt change in mineral assemblages and textures between both lithologies are more than obvious. It is unlikely to crystallize the VHK KREEP clasts with different mineral inventories and grain-sizes from the same shock-induced melt as the matrix at such small spatial scale at the same ambient temperature. Heterogeneity of the matrix may be expected resulting from fractional crystalliza-

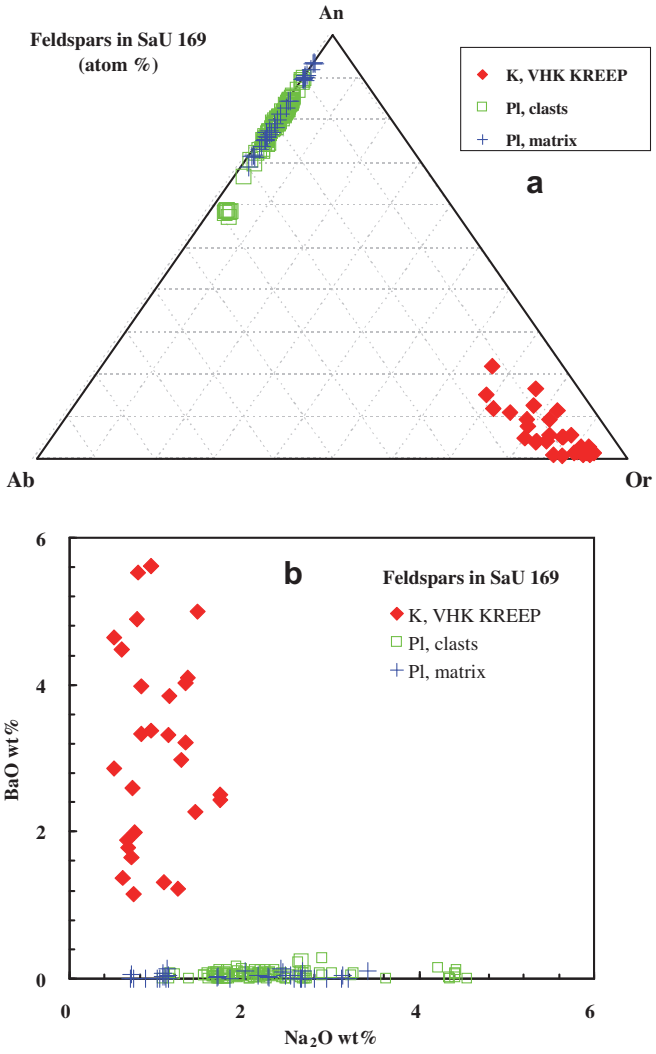

Fig. 12. Compositions of plagioclase and Ba-rich K-feldspar. Plagioclase grains (Pl) in the fine-grained matrix and those as clasts have the same compositions. K-feldspar (K) shows variable and high BaO-contents, with a narrower range of the Na_2O content relative to plagioclase.

tion, and the presence of the minor interstitial K-feldspar can be interpreted as the last liquidus mineral. However, except for the VHK KREEP clasts and other mineral clasts, the fine-grained matrix is rather homogeneous in the section studied. In fact, we found little variation in petrography and mineral chemistry among areas produced by fractional crystallization. In contrast, the high abundance of lithic and mineral clasts of the IMB (~25 vol.% this study, 25–40 vol.%, Gnos et al., 2004) and the presence of abundant relict cores of plagioclase in the matrix is indicative of a small volume of the shock-induced melt. Volume percent of the unmelted materials may be higher, because a part of pyroxene grains in the matrix could have relict cores as plagioclase. Such a mixture of solids and melt is not in favor of fractional crystallization. On the other hand, the coarse-grained textures of the VHK KREEP clasts (e.g. Fig. 4a) are not consistent with crystallization from a same melt of the fine-grained matrix either.

4.2. Petrogenesis of the VHK KREEP lithology

4.2.1. Modal and bulk compositions of the VHK KREEP lithology

Because of heterogeneity of the VHK KREEP clasts due to their coarse-grained nature and their presence in relatively small areas, the average bulk composition of the VHK KREEP clasts, instead of those of the individual ones, were calculated from their modal abundances of minerals and average mineral chemistries in the VHK KREEP clasts. The modal abundances of minerals were determined from their total surface areas of all VHK KREEP clasts described in the previous section of Petrography, which were converted to the weight percents according to densities of the phases. As depicted in Section 3.3, most of the minerals (except K-feldspar and a few pyroxene clasts) are rather homogeneous. Ilmenite was not quantitatively analyzed in this study, instead literature data (Gnos et al., 2004) were used. In addition,

Table 3
Representative analyses of phosphates, in wt%.

	Apatite						Merrillite							
	VHK KREEP		Matix		Metal-clasts		Clast		VHK KREEP		Matix		Metal-clasts	
MgO	0.14	0.17	0.14	0.73	0.16	0.09	3.24	3.19	3.52	3.36	3.45	3.37	3.45	3.64
Na_2O	b.d.	b.d.	b.d.	b.d.	0.03	b.d.	0.71	0.73	0.82	0.60	0.61	0.66	0.54	1.18
FeO	0.70	0.84	0.61	0.59	1.39	2.34	0.82	0.87	1.16	0.94	1.11	1.14	1.26	1.56
P_2O_5	41.2	41.9	41.9	40.6	41.5	41.3	45.4	45.5	44.7	45.0	44.7	44.9	45.0	46.6
Y_2O_3	b.d.	b.d.	b.d.	b.d.	b.d.	b.d.	2.25	2.14	2.24	2.57	2.50	2.34	2.47	1.21
La_2O_3	b.d.	b.d.	b.d.	b.d.	b.d.	b.d.	0.83	0.77	0.79	0.92	1.06	0.80	0.97	0.32
CaO	54.8	54.7	53.9	53.0	55.1	53.6	43.9	43.3	42.2	42.2	42.1	42.2	42.5	45.8
SiO_2	0.49	0.51	0.49	1.57	0.95	0.54	b.d.	b.d.	0.05	b.d.	b.d.	b.d.	b.d.	b.d.
Ce_2O_3	0.06	0.09	0.08	0.07	0.15	0.17	1.94	2.04	2.05	2.40	2.53	2.46	2.60	0.84
Nd_2O_3	b.d.	b.d.	b.d.	b.d.	b.d.	b.d.	1.06	1.13	1.04	1.14	1.27	1.23	1.46	0.53
Cl	0.94	1.03	1.12	1.17	0.77	0.92	0.06	0.02	b.d.	0.01	b.d.	b.d.	0.01	0.01
F	2.75	2.90	3.09	2.88	2.36	2.93								
Total	99.79	100.85	99.75	99.18	101.26	100.44	100.3	99.7	98.5	99.1	99.4	99.1	100.2	101.7
Cations per formular unit														
MgO	0.018	0.021	0.018	0.092	0.020	0.011	0.915	0.907	1.010	0.967	0.992	0.969	0.984	0.988
Na_2O	0.000	0.000	0.000	0.000	0.004	0.000	0.261	0.270	0.306	0.224	0.228	0.247	0.200	0.417
FeO	0.049	0.059	0.043	0.042	0.096	0.165	0.130	0.139	0.187	0.152	0.179	0.184	0.202	0.238
P_2O_5	2.940	2.969	3.002	2.918	2.906	2.939	7.278	7.343	7.284	7.351	7.300	7.328	7.292	7.186
Y_2O_3	0.000	0.000	0.000	0.000	0.000	0.000	0.227	0.217	0.229	0.264	0.257	0.240	0.251	0.117
La_2O_3	0.001	0.001	0.001	0.001	0.001	0.001	0.058	0.054	0.056	0.066	0.075	0.057	0.069	0.022
CaO	4.948	4.903	4.893	4.813	4.890	4.833	8.907	8.845	8.703	8.725	8.702	8.717	8.716	8.939
SiO_2	0.042	0.043	0.042	0.133	0.079	0.045	0.000	0.000	0.010	0.000	0.000	0.000	0.000	0.000
Ce_2O_3	0.002	0.003	0.002	0.002	0.004	0.005	0.135	0.142	0.145	0.170	0.179	0.174	0.182	0.056
Nd_2O_3	0.000	0.001	0.000	0.000	0.000	0.000	0.072	0.077	0.071	0.079	0.087	0.085	0.100	0.034
Cl	0.134	0.147	0.160	0.168	0.108	0.131	0.019	0.006	0.000	0.003	0.000	0.000	0.003	0.003
F	0.733	0.767	0.828	0.772	0.617	0.778								

b.d., below detection.

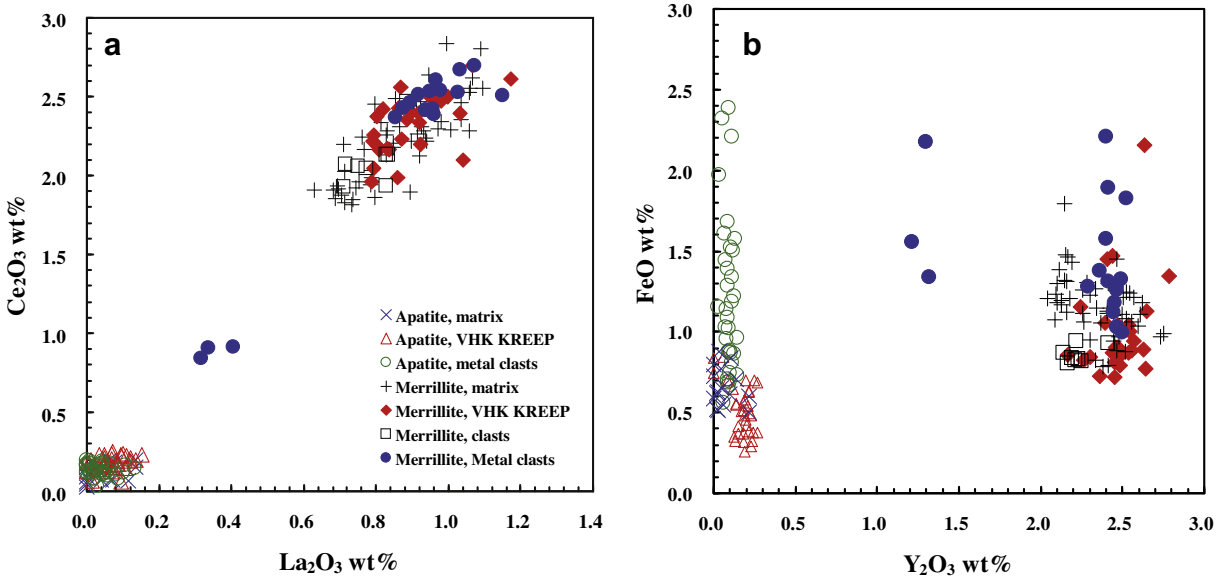

Fig. 13. Compositions of merrillite and apatite. Merrillite is more Y- and REE-rich than apatite. A few grains of merrillite coexisting with metal clasts contain significantly lower Y, La and Ce than those in the VHK KREEP clasts and the matrix.

the bulk composition of the matrix was calculated from its modal composition and average mineral chemistry as the VHK KREEP lithology. The calculated bulk compositions of the VHK KREEP clasts and the matrix are listed in Table 6 and plotted in Fig. 17, compared to the A-14 KREEP and the bulk IMB of SaU 169.

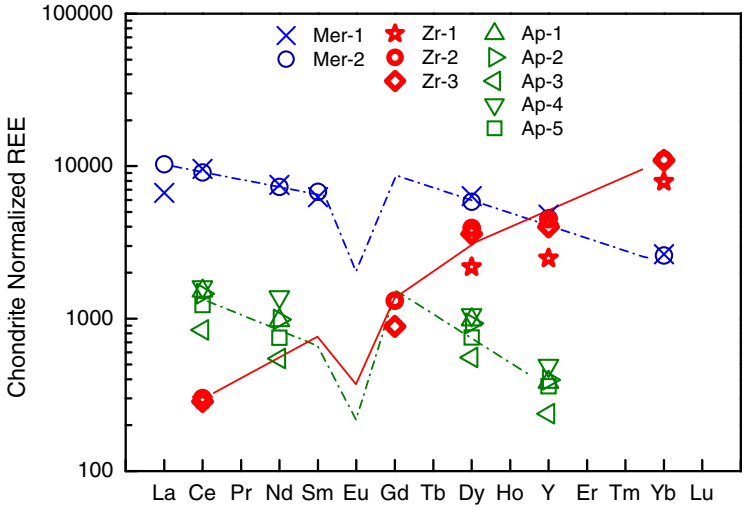

Fig. 14. CI-normalized REE patterns of merrillite, apatite, and zircon from SaU 169.

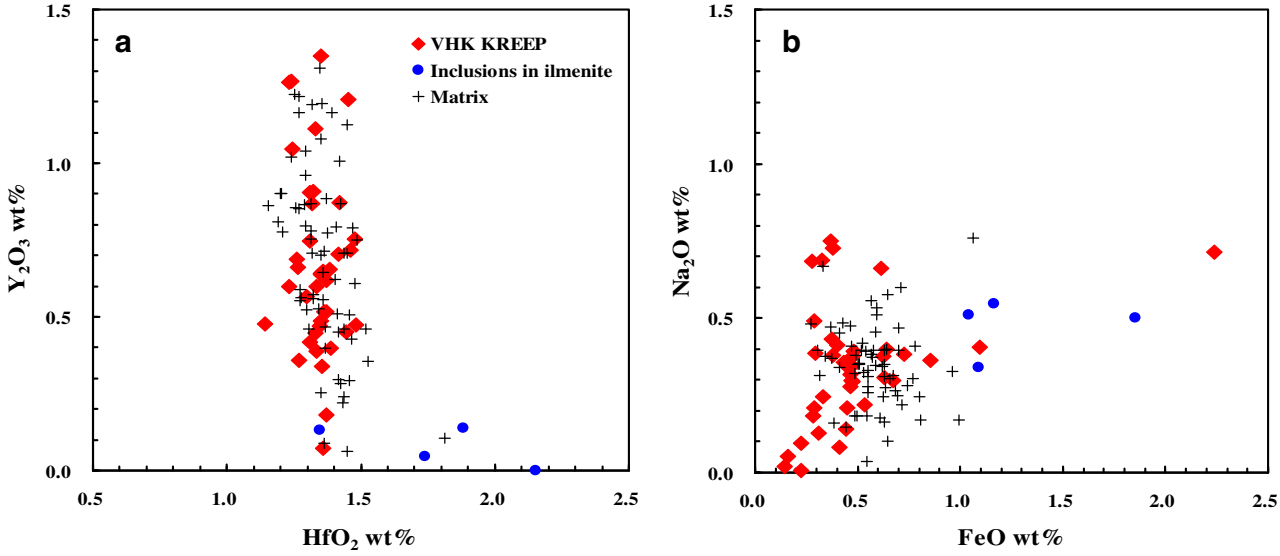

Fig. 15. Compositions of zircon. The grains in the VHK KREEP clasts and the fine-grained matrix overlap. A few inclusions in ilmenite have the lowest Y contents and higher HfO_2 and FeO contents, compared to the others.

It is evident that the VHK KREEP clasts are highly enriched in the KREEP component (e.g. K, REEs, P, Zr, Ba, Hf), by a factor of ~2 and 3 relative to the bulk SaU 169 IMB and the A-14 KREEP (Warren and Wasson, 1979), respectively. This is expected because the KREEP component in SaU 169 IMB is diluted by the abundant pyroxene and plagioclase clasts. More significantly, the VHK KREEP clasts are distinct from the bulk IMB and show no K-depletion in comparison with other incompatible elements. In fact, the VHK KREEP clasts are even slightly more K-enriched relative to the REEs and P (~4 × KREEP vs ~3.2–3.7 × KREEP). In addition, the VHK KREEP clasts contain very high Ba (7.2 × KREEP). Although over-estimation of Ba due to the spatial heterogeneity of K-feldspar cannot be entirely excluded, the KREEP-normalized Ba/K ratio of the VHK KREEP clasts (~1.8) is smaller than the ratio in SaU 169 IMB (~2.2) obtained from instrumental measurement (Gnos et al., 2004). Because both K and Ba are mainly present in K-feldspar, the high Ba concentration of the VHK KREEP clasts is probably intrinsic. The mg# of the VHK KREEP lithology is 0.63.

The VHK KREEP clasts contain the highest KREEP contents without K-depletion known to date. We infer these clasts most likely represent crystalline products from urKREEP. The SaU 169 IMB was reported to be the most KREEP-rich lunar mafic rock (Gnos et al., 2004), with

Table 4
Representative analyses of zircon and baddeleyite, in wt%.

	Zircon								Baddeleyite[b]	
	VHK KREEP			Matrix					Matrix	VHK KREEP
	1	2	3	4	5	6	7[a]	8[a]	9	10
MgO	b.d.	0.01	b.d.	b.d.	b.d.	b.d.	0.01	0.10	0.09	0.39
Na_2O	0.05	0.41	0.30	0.37	0.48	0.35	0.34	0.51	b.d.	0.03
FeO	0.16	1.09	0.68	0.37	0.27	0.51	1.09	1.04	1.56	1.18
TiO_2	0.08	0.07	b.d.	0.13	b.d.	0.08	0.90	0.64	3.14	1.20
ZrO_2	63.7	63.1	62.6	61.8	62.2	63.1	61.8	63.6	90.8	92.8
HfO_2	1.37	1.42	1.48	1.44	1.35	1.25	1.88	1.35	2.81	3.22
Y_2O_3	0.52	0.87	0.47	0.71	1.31	1.22	0.14	0.13	b.d.	b.d.
SiO_2	33.5	33.2	33.5	33.2	32.9	32.9	33.8	33.7	0.05	0.51
Al_2O_3	b.d.	b.d.	b.d.	0.03	b.d.	b.d.	0.60	b.d.	b.d.	0.26
CaO	0.03	0.06	0.18	0.11	0.05	b.d.	0.29	0.08	0.09	0.69
Total	99.7	100.4	99.4	98.3	98.9	99.6	101.0	101.5	99.6	101.1
Cations per formular unit										
Mg	0.000	0.001	0.000	0.000	0.000	0.000	0.000	0.004	0.003	0.011
Na	0.003	0.024	0.018	0.022	0.028	0.021	0.019	0.029	0.000	0.001
Fe	0.004	0.027	0.017	0.009	0.007	0.013	0.027	0.026	0.026	0.019
Ti	0.002	0.002	0.000	0.003	0.000	0.002	0.020	0.014	0.048	0.018
Zr	0.948	0.923	0.924	0.923	0.927	0.934	0.890	0.916	0.903	0.901
Hf	0.012	0.012	0.013	0.013	0.012	0.011	0.016	0.011	0.016	0.018
Y	0.008	0.014	0.008	0.011	0.021	0.020	0.002	0.002	0.000	0.000
Si	1.022	0.994	1.014	1.014	1.003	0.998	0.995	0.994	0.001	0.010
Al	0.000	0.000	0.000	0.001	0.000	0.000	0.021	0.000	0.000	0.006
Ca	0.001	0.002	0.006	0.004	0.002	0.000	0.009	0.003	0.002	0.015

[a] Included in ilmenite; b.d., below detection.
[b] Fe and Ti may be contaminated by ilmenite.

incompatible elements enriched by a factor of ~1.5–1.8 relative to the average Apollo 14 high-K KREEP proposed by Warren and Wasson (1979). However, the bulk IMB was K-depleted (~0.6 × KREEP) relative to REEs, P and other incompatible elements in high-K KREEP. Our observations confirm that SaU 169 IMB contains abundant various lithic and mineral clasts (Gnos et al., 2004), in addition to a new type of lithic clasts, i.e. the VHK KREEP clasts encountered during the present investigations. These clasts contain abundant Ba-bearing K-feldspar instead of plagioclase encountered in the matrix, and hence the clasts are K-enriched.

Very few superKREEP compositions have been reported in the literature, e.g. 15405c quartz monzodiorite (QMD) clasts (Warren, 1988; Marvin et al., 1991), 14161 QMD clasts (Jolliff, 1991) and 14313,34 white clast (Haskin et al., 1973). However, they are silica-bearing and very SiO_2-enriched ($\geqslant$56.4 wt%). These superKREEP lithologies were likely produced mainly by high fractional crystallization of a KREEPy basaltic magma (Marvin et al., 1991; Rutherford et al., 1996). In addition, lunar granites probably experienced crystal–liquid fractionation and/or liquid immiscibility. In contrast, the VHK KREEP clasts found in SaU 169 are mafic, consisting of only 48.3 wt% SiO_2 in addition to 15.6 wt% FeO and 14.7 wt% MgO with mg# value of 0.63 (Table 6). As shown in Table 6, the SiO_2-content of the VHK KREEP clasts is almost the same as that of the A-14 KREEP (47.9 wt%), whereas the FeO and MgO contents are significantly higher than those of the latter (10.5 and 10.6 wt%, respectively). In addition, the VHK KREEP clasts contain lower Al_2O_3, CaO and Na_2O than the A-14 KREEP, mainly due to the presence of K-feldspar in the former while plagioclase in the latter. The very high concentrations of incompatible elements of the VHK KREEP clasts could unlikely have evolved from fractional crystallization from A-14 KREEP basaltic magmas, which is expected to produce a silica-rich residual melt with lower FeO and/or MgO.

The VHK KREEP clasts probably represent a new type of lunar rocks. They show coarse-grained texture, and occur as clasts in the fine-grained matrix of the SaU 169 IMB. These VHK KREEP clasts consist mainly of pyroxenes and Ba-rich K-feldspar with less abundant phosphates, ilmenite, zircon and minor plagioclase. No silica mineral was encountered in them, consistent with the mafic bulk composition. This is significantly different from the superKREEP quartz monzodiorite clasts (Jolliff, 1991; Marvin et al., 1991). Other known K-feldspar-rich lunar rocks are felsites or lunar granites which contain K_2O up to 3.39–8.6 wt% (Seddio et al., 2010). However, they are characterized by high enrichment in SiO_2 (68.1–75.5 wt%) and are silica-bearing with very low FeO (0.9–6.99 wt%) and MgO (<1.53 wt%) contents (Seddio et al., 2010).

4.2.2. Composition of urKREEP

The composition of VHK KREEP lithology could be the most close to that of urKREEP up to date because it was not significantly diluted by Mg-rich magmas. In fact, the VHK KREEP clasts are almost composed of K-REE-P-rich minerals, i.e. K-feldspar (K), phosphates (REEs, P)

Table 5
SIMS Pb–Pb analyses of zircon and baddeleyite (grains in the VHK KREEP clasts).

Analysis	Size (μm)	Surface	$^{204}Pb/^{206}Pbm$	$\pm1\sigma$ (%)	$f^{206}Pbc$ (%)	$^{207}Pb/^{206}Pbm$	$\pm1\sigma$ (%)	$^{207}Pb/^{206}Pbc$	$t_{207/206}$ (Ma)	$\pm2\sigma$
4[a]	23 × 5		6.58E−04	12	0.92	0.4150	0.61	0.4068	3934.6	16.7
1-1	47 × 32	Fractured	1.08E−05	57	0.02	0.4162	0.32	0.4132	3957.7	16.7
1-2		Smooth	8.52E−04	8	1.19	0.4035	0.42	0.3937	3885.1	16.7
1-3		Smooth	9.62E−04	9	1.35	0.4120	0.54	0.4013	3913.9	16.7
3	30 × 7	Smooth	5.72E−04	13	0.80	0.4341	0.59	0.4267	4005.9	16.6
5-1	45 × 35	Fractured	7.68E−04	8	1.07	0.4097	0.45	0.4006	3911.5	16.7
5-2		Smooth	1.67E−04	15	0.23	0.4082	0.40	0.4039	3923.7	16.7
5-3		Smooth	2.92E−04	12	0.41	0.4088	0.40	0.4035	3922.3	16.7
6	45 × 25	Smooth	9.70E−04	9	1.36	0.4117	0.53	0.4009	3912.6	16.7
7	14 × 10	Smooth	6.90E−04	10	0.97	0.4189	0.48	0.4105	3947.9	16.7
12	23 × 13	Smooth	7.71E−04	9	1.08	0.4078	0.46	0.3987	3904.2	16.7
13-1	30 × 20	Fractured	1.33E−03	8	1.86	0.4521	0.48	0.4391	4048.8	16.6
13-2		Smooth	1.65E−04	19	0.23	0.4246	0.47	0.4204	3983.5	16.6
13-3		Fractured	5.77E−04	9	0.81	0.4069	0.42	0.3994	3906.8	16.7
14-1	50 × 27	Fractured	1.25E−03	9	1.75	0.4185	0.59	0.4056	3929.9	16.7
14-2		Fractured	1.19E−03	11	1.66	0.4083	0.71	0.3958	3893.0	16.7
14-3		Fractured	7.36E−04	12	1.03	0.4157	0.62	0.4069	3934.9	16.7
14-4		Smooth	5.37E−04	10	0.75	0.4041	0.48	0.3969	3897.3	16.7
14-5		Smooth	4.78E−04	12	0.67	0.4330	0.49	0.4263	4004.4	16.6
15-1	50 × 32	Fractured	1.12E−04	21	0.16	0.4321	0.42	0.4282	4011.2	16.6
15-2		Smooth	7.20E−04	10	1.01	0.4132	0.52	0.4045	3925.8	16.7
16-1	25 × 20	Smooth	7.14E−04	9	1.00	0.4072	0.45	0.3985	3903.5	16.7
16-2		Smooth	2.83E−04	12	0.40	0.4063	0.39	0.4011	3913.2	16.7
16-3		Smooth	9.72E−04	10	1.36	0.4174	0.61	0.4068	3934.2	16.7
8-1	112 × 40	Fractured	6.81E−04	10	0.95	0.4143	0.52	0.4059	3931.0	16.7
8-2		Smooth	1.12E−03	9	1.56	0.4153	0.56	0.4034	3921.7	16.7
8-3		Smooth	3.25E−04	14	0.45	0.4063	0.57	0.4008	3912.0	16.7
8-4		Smooth	7.51E−04	10	1.05	0.4125	0.54	0.4036	3922.4	16.7
8-5		Smooth	7.89E−04	14	1.10	0.4226	0.71	0.4135	3958.8	16.7
8-6		Smooth	8.03E−04	9	1.12	0.4071	0.49	0.3977	3900.5	16.7
8-7		Smooth	6.73E−04	24	0.94	0.4159	1.18	0.4076	3937.3	18.7
10-1	118 × 20	Smooth	3.89E−04	14	0.54	0.4071	0.54	0.4011	3913.3	16.7
10-2		Smooth	1.36E−03	10	1.90	0.4167	0.71	0.4028	3919.7	16.7
10-3		Smooth	1.99E−03	9	2.79	0.4566	0.73	0.4388	4047.5	16.6
10-4		Smooth	6.93E−04	13	0.97	0.4335	0.59	0.4251	4000.4	16.6
10-5		Smooth	1.33E−03	11	1.86	0.4444	0.73	0.4313	4021.9	16.6
11-1	50 × 23	Smooth	2.20E−04	13	0.31	0.4092	0.34	0.4046	3926.1	16.7
11-2		Smooth	3.44E−04	11	0.48	0.4079	0.40	0.4022	3917.4	16.7
17-1	102 × 8	Smooth	5.66E−04	10	0.79	0.4131	0.44	0.4057	3930.2	16.7
17-2		Smooth	4.61E−04	9	0.65	0.4093	0.38	0.4027	3919.3	16.7
18	100 × 41	Smooth	1.69E−04	16	0.24	0.4056	0.43	0.4013	3914.1	16.7
19	45 × 25	Smooth	4.97E−04	12	0.70	0.4126	0.45	0.4057	3930.5	16.7

Abbreviation: m, measured; c, corrected for common lead; f, percent of common ^{206}Pb.

[a] Baddeleyite, others are zircon.

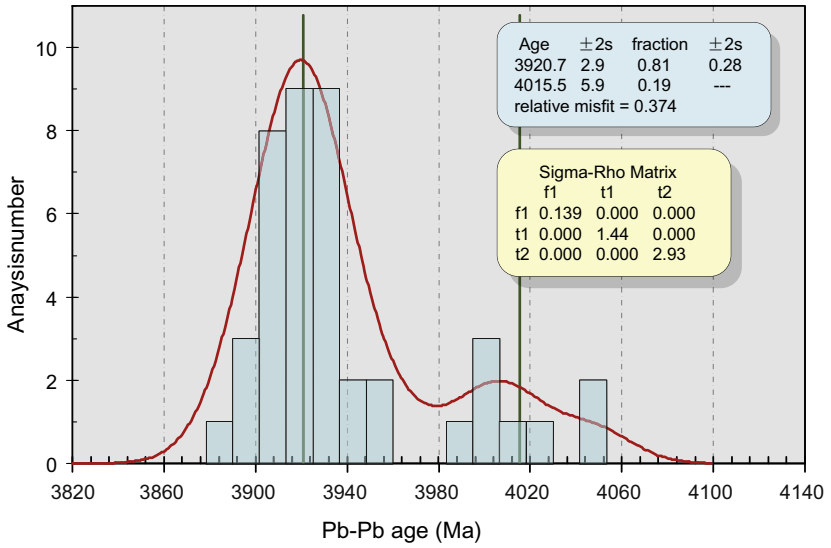

Fig. 16. Histogram of Pb–Pb ages of zircon and baddeleyite from SaU 169 IMB, showing a dichotomy. The major peak occurs at 3921 ± 3 Ma (2σ) and a smaller one at 4016 ± 6 Ma (2σ).

Table 6
Bulk compositions of the VHK KREEP clasts and the matrix, normalized to 100 wt%.

Location	VHK KREEP	Matrix	IMB-25% clast[a]	Clast-free IMB[b]	IMB[c]	A-14 KREEP[d]
SiO_2	48.25	45.21	45.29	44.40	45.15	47.92
Al_2O_3	5.26	11.63	15.68	10.90	15.88	16.63
FeO	15.65	13.75	10.39	14.00	10.67	10.55
MnO	0.221	0.192	0.140		0.140	0.139
MgO	14.68	12.41	10.91	12.20	11.09	10.61
CaO	4.17	8.30	10.77	7.40	10.16	9.51
Na_2O	0.313	0.678	0.933	0.800	0.980	0.863
K_2O	2.733	0.543	0.627	0.400	0.540	0.831
TiO_2	3.406	3.658	2.844	4.900	2.210	1.668
ZrO_2	1.115	0.381	0.484		0.380	0.230
BaO	0.784	0.154	0.201	0.140	0.170	0.134
Cr_2O_3	0.168	0.161	0.160		0.140	0.190
P_2O_5	2.405	2.145	1.475	2.000	1.140	0.779
Y_2O_3	0.123	0.122	0.088		0.068	
La_2O_3	0.041	0.044	0.026		0.020	
Ce_2O_3	0.104	0.113	0.065		0.050	
Nd_2O_3	0.055	0.059	0.039		0.030	
HfO_2	0.024	0.008	0.010		0.008	
Nb_2O_5	0.037	0.040	0.023		0.018	
mg#	0.63	0.62		0.61	0.65	0.64

The whole IMB can be simply referred to as a mixture of the matrix and clasts.
[a] Subtracted 25 vol.% clasts from the bulk composition of the IMB[c].
[b] Calculated bulk composition of clast-free IMB (Gnos et al., 2006).
[c] The measured bulk composition of the IMB (Gnos et al., 2004).
[d] The referred KREEP composition (Warren and Wasson, 1979).

and zircon (HREEs), but not pyroxenes. Taking the extreme case into account that all pyroxenes (the only components in the VHK KREEP clasts have little contribution to K, REEs or P) could have been contributed by the Mg-rich magma, the concentrations of KREEP component in the VHK KREEP parental magma would then be diluted by a maximum factor of ~2.2. Alternatively, the "Standard Initial" (SI) melt (with a mg# of 0.80, Warren, 1988) was taken as the possible Mg-rich magma mixed with urKREEP. Assuming a simple model of two-magma mixture the majority of MgO could have been contributed from the SI melt, the composition of the proposed urKREEP could then be deduced from that of the VHK KREEP lithology by mass balance, which contains 50.9 wt% SiO_2 and 19.3 wt% FeO with the concentration of KREEP component enhanced by a factor of 2. Both calculations reveal a

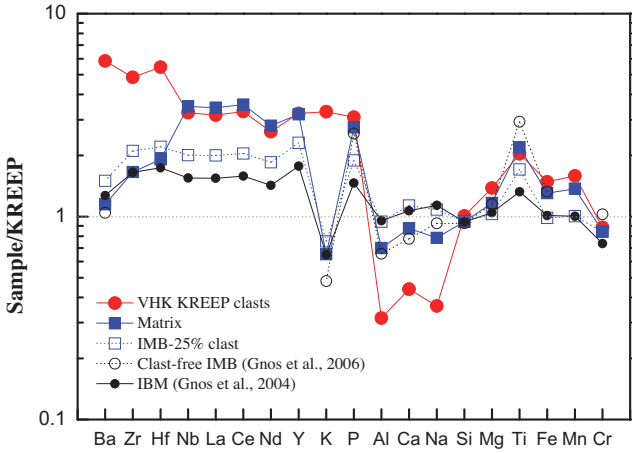

Fig. 17. KREEP-normalized bulk compositions of VHK KREEP clasts and the fine-grained matrix, compared to those of the IMB (Gnos et al., 2004) and clast-free IMB (Gnos et al., 2006). The IMB-25% clast was calculated from the bulk composition of the IMB subtracted 25% of the lithic and mineral clasts. Note K-depletion in all except for the VHK KREEP clasts. The bulk composition of KREEP is from Warren and Wasson (1979).

similar maximum concentration of the KREEP component of urKREEP.

The above estimations could be referred to as extreme cases. The composition of urKREEP may be more similar to that of the VHK KREEP lithology, although its mg# (0.63) is much higher than ~0 expected for the final residuum of the lunar magma ocean by Warren (1988). Recent calculation of the solidification process of the lunar magma ocean resulted in higher mg# of ~0.35–0.6 for the last liquids (1–10%), which is much enhanced due to gravitationally-driven overturn (Elkins-Tanton et al., 2011). On the other hand, the higher mg# of the VHK KREEP lithology than the expected value of urKREEP may partly result from removing some ilmenite from the parental magma of the VHK KREEP lithology due to its high density. Ilmenite that began to crystallize from ferrobasaltic magmas as K_2O concentration increased up to 1.6–2.2 wt% (Hess et al., 1978) before reaching the K_2O concentration of the VHK KREEP clasts (2.7 wt%).

When normalized to the KREEP composition of Warren and Wasson (1979), the SaU 169 IMB is K-depleted by a factor of ~3 relative to REEs, P and other incompatible trace elements (Fig. 17). The K-depletion is not due to dilution by various mafic rock clasts and crystal clasts that are poor in REEs, P and other ITE. SaU 169 IMB can be referred to as a mixture of a pre-impact REEP-rich lithology and abundant mafic and mineral clasts plus minor VHK KREEP clasts. The fine-grained matrix may represent a composition of the pre-impact REEP-rich lithology, without assimilating significant amounts of various clasts during the shock event. This assumption seems to be reasonable, because the presence of abundant relict cores in the matrix plagioclase suggests a low degree of melting as demonstrated above. The bulk composition of the matrix was calculated from both the modal composition and the average mineral chemistry. It was also obtained by subtracting lithic and mineral clasts from the measured SaU 169 IMB composition (Gnos et al., 2004). Both KREEP-normalized calculations are consistent with each other (Table 6), showing significant K-depletion (Fig. 17).

With exception of the fine-grained texture, the very low abundance of K-feldspar and the related K-Ba-depletion, the fine-grained matrix, i.e. the pre-impact REEP-rich lithology, is rather similar to the VHK KREEP clasts in mineral chemistry and the REEP-enriched bulk compositions. Especially, the compositions of pyroxene, phosphates and zircon in both lithologies are indistinguishable as demonstrated above, thus suggesting a genetic relationship between them. However, the VHK KREEP clasts, being lithic in nature, cannot have been produced by fractional crystallization of the shock-induced melt as discussed above. On the other hand, it is unlikely to produce the matrix by mixing the VHK-KREEP lithology with various clasts of pyroxene and plagioclase during the catastrophic shock event, because this assimilation would have diluted the concentrations of K-REE-P with the same proportion. In addition, petrographic textures show little volatile loss of K during the shock-induced melting. In contrast, the minor K-feldspar in the matrix occurs as the last liquidus phase instead of the residue of volatilization as discussed above. The K-depletion of the matrix relative to the VHK KREEP lithology suggests a K-decoupling process perhaps controlling the formation of the matrix. However, the proposed K-decoupling process remains unclear.

Yet, K-decoupling is not rare in lunar KREEPy samples. Warren and Wasson (1979) noted variation of K in KREEPy samples (>0.1 × REEP) at all five Apollo landing sites, while other incompatible trace element patterns showed no resolvable variation. Silicate liquid immiscibility (SLI) of KREEP melts was proposed as a possible mechanism for K-decoupling, which produced high-K granites and REEP-rich mafic melts (Neal and Taylor, 1988; Snyder et al., 1991; Jolliff et al., 1999). This scenario explains the presence of lunar granites and the glass in lunar soil. In addition, VHK basalts contain elevated K_2O contents, probably produced by assimilating high-K granites

(Shervais et al., 1985; Warren et al., 1986; Neal et al., 1989a,b). However, the REEP-rich mafic melts produced by SLI is expected to be FeO-enriched and to crystallize fayalite (Neal and Taylor, 1988), different from the petrography and bulk composition of the fine-grained matrix of SaU 169 IMB.

4.3. Multi-impact events and shock metamorphism

A previous study concluded that SaU 169 experienced four lunar impact events at 3909 ± 13, ~2800, ~200, and <0.34 Ma (Gnos et al., 2004), and the IMB lithology was formed and metamorphosed by the first two events, respectively. Our petrographic observations of the SaU 169 IMB suggest a more complicated shock history.

As discussed above, the VHK KREEP lithology predated the fine-grained matrix that was produced by a severe shock-induced melting at 3909 ± 13 Ma dated with zircon grains in the matrix (Gnos et al., 2004). The coarse-grained texture of the VHK KREEP lithology indicates crystallization from a larger magma pool than the post shock melt of the matrix. The parental magma of the VHK KREEP lithology may represent the last residuum of the lunar magma ocean with possible dilution by mafic rocks. In this case, older ages of zircon in the VHK KREEP clasts relative to those in the matrix are expected. Solidification of the lunar magma ocean was reported before ~4.0 Ga based on zircon U–Pb dating (Nemchin et al., 2008) or 4.3 based on thermal models of the lunar magma ocean (Meyer et al., 2010). However, the analyses of many zircon grains in the VHK KREEP clasts and the matrix reveal no difference in the Pb–Pb ages (see Section 4.4). Alternatively, the VHK KREEP magma was produced from mixtures of the urKREEP component and mafic rocks by a catastrophic impact event predated the SaU 169 IMB. The similar zircon Pb–Pb ages between the VHK KREEP clasts and the matrix indicate the two impact events took place within a period of a few million years.

The fine-grained matrix crystallized from the shock-induced melt. The analyses of a number of zircon grains with various morphologies and habits (crystalline and amorphous, zoned and unzoned) and one baddeleyite show a major peak at 3921 ± 3 Ma (see Section 4.4), confirming the age of the catastrophic shock event (Gnos et al., 2004; Liu et al., 2009). This impact event partially melted and mixed up the precursors of SaU 169 IMB, *i.e.* the pre-impact REEP-rich lithology (represented by the fine-grained matrix) and various lithic and mineral clasts. However, a large proportion of the precursor material remained unmelted as indicated by the presence of abundant mineral and lithic clasts (25 vol.% in this study and 25–40 vol.% reported by Gnos et al., 2004). Even the fine-grained matrix of the IMB did not all crystallize from the post shock melt, as evidenced from the occurrence of abundant relict grains as the cores of plagioclase.

After solidification, the IMB was heavily shocked by another impact event at ~2.8 Ga based on Ar–Ar dating of a feldspar concentrate from the IMB (Gnos et al., 2004). This event transformed plagioclase of both the mineral clasts and the fine-grained matrix to diaplectic glass. Relict crystalline inclusions commonly remain in large plagioclase clasts, as indicated by presence of the fractured regions with different CL (Fig. 7b–d) and confirmed by the Raman spectra of plagioclase. The dense and thin lamellae revealed by CL in the relict islands of plagioclase clasts (e.g. Fig. 7d) probably indicate presence of polysynthetic twinning.

The majority of zircon grains have been transformed to amorphous phase based on Raman spectra. Amorphization of zircon can be due to radiation damage (Meldrum et al., 1998), because the SaU 169 zircon grains contain high U (161–294 ppm) and Th (35–288) (Liu et al., 2009) and have an age of 3.9 Ga. However, as described above, the characteristic Raman bands of zircon (e.g. 1008 cm^{-1}) were always observed in the fractured areas of a few large grains, but absent in the predominant smooth regions. This is confirmed by mapping the intensity of 1008 cm^{-1} band of the Raman spectra on the largest zircon grain (Figs. 3c and 9c), showing the spatial coherence of the presence of 1008 cm^{-1} peak and the fractured area of the grain. Metamictization due to radiation damage would have been identified in the whole zircon grains, including the fractured areas. In contrast, the observations of zircon are similar to the shocked features of the plagioclase clasts. Hence, the amorphous zircon grains were shock-induced, i.e. they are diaplectic glass. Amorphous zircon grains have been reported in a complex zircon assemblage from lunar breccia 73235 (Pidgeon et al., 2007). The assemblage consists of a fine network matrix of zircon that was transformed to diaplectic glass and many primary clasts that still retain a crystalline state. Shock experiments show that the Raman peaks of zircon vanish at 60 GPa (Gucsik et al., 2002) or lower pressures of 38–40 GPa (Gucsik et al., 2004; Wittmann et al., 2006). However, the shock experiment results are inapplicable to estimate P–T conditions of SaU 169 IMB, because of very short duration achieved by the dynamic experiments and the unrealistic high-pressure applied in dynamic experiments. In contrast, the P–T conditions of the diaplectic glass of zircon can be constrained according to static high-pressure experiments. Absence of reidite the high-pressure polymorph of zircon suggests a pressure of <9 GPa at ~1200 K, based on the phase diagram of zircon–reidite (Ono et al., 2004). The absence of reidite is unlikely due to retrograde reactions, because both diaplectic glasses of zircon and plagioclase show little recrystallization. The low shock-induced pressure is consistent with the absence of other high pressure polymorphs, e.g. ringwoodite, majorite or lingunite in the sample, and no decomposition of zircon to ZrO_2 (cotunnite structure) and SiO_2 (stishovite), which takes place at pressures of >20 GPa (Ono et al., 2004; Tange and Takahashi, 2004).

Several shock-melt pockets and fine melt veins were observed in the section (Fig. 8), probably formed together with the diaplectic glass of zircon and plagioclase by the same impact event. However, the common occurrence of abundant vesicles in the melt pockets indicates degassing under very low pressure during the shock-induced melting or alternatively, that melting took place after decompression due to high post-shock temperatures. This post-shocked low pressure condition conflicts with that required to form diaplectic glass of plagioclase and zircon, hence the

melt pockets and probably the melt veins may indicate the presence of a distinct impact event.

4.4. Dating of the VHK KREEP lithology and shock events

As discussed above, at least three main events have been recognized based on the petrographic features of the SaU 169 IMB: (1) crystallization of the VHK KREEP lithology, (2) shock-induced melting of the IMB matrix, and (3) transformation of the crystalline zircon to diaplectic glass. These events can be dated by Pb–Pb analysis conducted on the retained crystalline parts and the diaplectic areas of zircon grains in the VHK KREEP clasts and the matrix. In addition, a few large grains of zircon in the VHK KREEP clasts show various CL zonings (Figs. 3–5), probably recorded multi-episode magmatism. However, no difference of the Pb–Pb ages was found between the CL zonings, probably due to the very thin CL zonings (<4 μm) and/or a short period of crystallization.

All analyses of the retained crystalline parts and the diaplectic glass areas of zircon grains in both VHK KREEP clasts and matrix show no distinct Pb–Pb age distributions related to the different petrographic settings and/or the crystal features (Table 5). Majority of the Pb–Pb ages cluster at a peak of 3921 ± 3 Ma, consistent with the previous zircon Pb–Pb age of 3909 ± 13 Ma (Gnos et al., 2004) and the U–Pb age of 3920 ± 13 Ma (Liu et al., 2009). In addition, 8 out of 41 analyses have Pb–Pb ages >3980 Ma with an average of 4015 ± 6 Ma (Fig. 16).

Similarity of the Pb–Pb ages between the retained crystalline parts and the diaplectic areas of zircon reveals no resetting when the zircon grains were shocked to diaplectic glass, which took place probably at ~2800 Ma based on Ar–Ar dating of maskelynite (Gnos et al., 2004). This is confirmed by the absence of a tail towards 2.8 Ga in the Pb–Pb age distribution (Fig. 16) and the same Pb–Pb age of 3935 ± 17 Ma of a crystalline baddeleyite (Table 5) within the analytical uncertainties. Another line of evidence is the concordia U–Pb ages of zircon (Liu et al., 2009), which indicates little disturbance of the zircon U–Pb system. Although no petrographic settings or crystal features of the zircon grains were reported in the previous studies, the analyses were likely conducted on the most abundant diaplectic glass of zircon from the same meteorite. Another interpretation of absence of the resetting is that these grains were transformed to diaplectic glass by a distinct impact event that took place within a few million years after the IMB formation. Disturbance of the U–Pb system were reported in a few lunar zircon grains attributed to severe shock events (Pidgeon et al., 2007, 2011).

SaU 169 IMB was formed by a catastrophic shock event, by making a mixture of the post shock melt with large amounts of various lithic and mineral clasts. This impact event was dated with zircon crystallized from the shock-induced melt of the matrix. Our analyses of Pb–Pb ages of zircon grains in the matrix show an average age of 3923 ± 7 Ma (excluding analyses >3980 Ma), consistent with the previous Pb–Pb age of 3909 ± 13 Ma (Gnos et al., 2004) and U–Pb age of 3920 ± 13 Ma (Liu et al., 2009). The VHK KREEP lithology predated the matrix based on the petrographic observations. However, the Pb–Pb ages of the zircon grains in the VHK KREEP clasts are identical to those in the matrix within the analytical uncertainties, with an average age of 3918 ± 9 Ma (excluding analyses >3980 Ma). One possibility is that the zircon Pb–Pb ages of the VHK KREEP clasts have been completely reset by the later shock event that melted the matrix. However, the zircon grains in the VHK KREEP clasts show no evidence for more severe metamorphism than those in the matrix. In fact, the large zircon grains in the VHK KREEP clasts commonly retain the crystal structure. Alternatively, crystallization of the VHK KREEP lithology took place very close, i.e. less than a few million years, to the catastrophic shock event at ~3.92 Ma.

The older Pb–Pb ages (3980–4050 Ma) of a few zircon grains in both lithologies reveal presence of relict crystals. This is consistent with the previous report of an older bulk U–Pb age of 4290 ± 30 Ma (Kramers et al., 2007), which was explained as a mixture of zircon crystallized from the impact melt at 3.9 Ga and much smaller and older crystals.

5. CONCLUSIONS

We encountered a new type of lithic clasts of the VHK KREEP lithology in the impact melt breccia of lunar meteorite SaU 169. It mainly consists of Ca-poor and Ca-rich pyroxenes and Ba-rich K-feldspar with less abundant phosphates, ilmenite and zircon. Except for pyroxenes, all other components are K/REE/P-bearing phases. The bulk composition of the VHK KREEP lithology was determined from the modal abundances of minerals and the average mineral chemistry, and it is the most KREEP-rich (~1500 × CI) mafic rock up to date. The VHK KREEP lithology is probably a sample most similar to the postulated urKREEP, but slightly diluted by Mg-rich magma with a factor <2.2.

The bulk compositions of the IMB and the fine-grained matrix are K-depleted relative to REEs, P and other incompatible trace elements. The proposed K-decoupling is not due to silicate liquid immiscibility of the shock-induced melt, because both the matrix and the VHK KREEP lithology have compatible bulk concentrations of SiO_2, FeO and MgO. The similar mineral chemistry and mineral assemblages among the matrix and the VHK KREEP lithology, except for the presence of plagioclase in the former and Ba-rich K-feldspar in the latter, suggest a genetic relationship among them. However, the K-depletion of the matrix cannot be explained by simple mixing the VHK KREEP lithology with mainly anorthosite during the catastrophic impact event. This scenario should have reduced the relative abundances of phosphates, ilmenite and zircon as well. The causes of the observed K-decoupling in the matrix remain unknown so far.

The SaU 169 IMB experienced a multi-stage shock episode. Based on petrography, at least three main impact events can be recognized. The first catastrophic event took place at 3.92 Ga and produced a mixture of shock-induced melt with a large amount of various clasts, which crystallized to form the SaU 169 IMB. The second impact event, dated 2.8 Ga based on Ar–Ar analysis of the diaplectic

glass of plagioclase (Gnos et al., 2004), transformed most plagioclase and probably zircon to diaplectic glass, with only small crystalline areas preserved in a few large grains of plagioclase and zircon. The absence of reidite (a high-pressure polymorph of zircon) suggests a pressure of <9 GPa at ~1200 K based on the zircon–reidite phase diagram (Ono et al., 2004). Finally, presence of shock-induced vesiculous melt pockets indicates a very low-pressure condition, distinct from the diaplectic glass-forming event. These melt pockets were produced at ambient pressure and high post shock temperature after decompression probably by a third impact event.

The Pb–Pb ages of zircon with various settings and one baddeleyite grain were analyzed with CAMECA ism 1280. Our analyses show a bimodal pattern with a major peak at 3921 ± 3 Ma and a small peak at 4016 ± 6 Ma. The major peak at 3921 ± 3 Ma is identical to the previous zircon Pb–Pb dating by Gnos et al. (2004) and U–Pb dating by Liu et al. (2009). The older Pb–Pb ages of a few zircon grains are consistent with the previous report of an older bulk U–Pb age of 4290 ± 30 Ma (Kramers et al., 2007), which reveals presence of relict crystals in both lithologies. Furthermore, the zircon Pb–Pb ages conducted on the retained crystalline parts and the diaplectic glass are undistinguishable from each other, suggestive of no resetting by the later impact event at ~2.8 Ga or there was another severe impact event took place within a few million years after solidification of the matrix. The VHK KREEP lithology predated the matrix, but has the same zircon Pb–Pb ages of the latter within the analytical uncertainties. This similarity suggests that the VHK KREEP lithology crystallized just before the catastrophic shock event not earlier than a few million years. Although complete resetting of the zircon Pb–Pb ages of the VHK KREEP clasts by the later catastrophic impact events cannot be excluded, these zircon grains show no evidence for more severe shock metamorphism than those in the matrix.

ACKNOWLEDGMENTS

The manuscript has been significantly improved by the constructive reviews by E. Gnos and an anonymous reviewer, and the helpful comments by C. Koeberl the Associate Editor. The authors are also grateful to C.R. Neal and A. El Goresy for their incisive comments and suggestions. This study was supported by the Knowledge Innovation Program of Chinese Academy of Sciences (Grant No. KZCX2-YW-Q08), the National 863 High-Tech R&D Program of China (Grant No. 2009AA122201) and the Pre-planed Projects of Lunar Sample Analysis (Grant No. TY3Q20110029).

REFERENCES

Elkins-Tanton L. T., Burgess S. and Yin Q.-Z. (2011) The lunar magma ocean: reconciling the solidification process with lunar petrology and geochronology. *Earth Planet. Sci. Lett.* **304**, 326–336.

Gnos E., Hofmann B. A., Al-Kathiri A. and Whitehouse M. J. (2006) The KREEP-rich Imbrium impact melt breccia of the lunar meteorite Sayh Al Uhaymir 169. *Meteorit. Planet. Sci.* **41**, #5111 (abstr.).

Gnos E., Hofmann B. A., Al-Kathiri A., Lorenzetti S., Eugster O., Whitehouse M. J., Villa I. M., Jull A. J. T., Eikenberg J., Spettle B., Krähenbühl U., Franchi I. A. and Greenwood R. C. (2004) Pinpointing the source of a lunar meteorite: implications for the evolution of the Moon. *Science* **305**, 657–659.

Gucsik A., Koeberl C., Brandstätter F., Reimold W. U. and Libowitzky E. (2002) Cathodoluminescence, electron microscopy, and Raman spectroscopy of experimentally shock-metamorphosed zircon. *Earth Planet. Sci. Lett.* **202**, 495–509.

Gucsik A., Zhang M., Koeberl C., Salje E., Redfern S. and Pruneda J. (2004) Infrared and Raman spectra of $ZrSiO_4$ experimentally shocked at high pressures. *Mineral. Mag.* **68**, 801.

Haskin L. A., Helmke P. A., Blanchard D. P., Jacobs J. W. and Telander K. (1973) Major and trace element abundances in samples from the lunar highlands. *Lunar Planet. Sci. Conf. Proc.* **4**, 1275–1296.

Hess P. C., Rutherford M. J. and Campbell H. W. (1978) Ilmenite crystallization in nonmare basalt – genesis of KREEP and high-Ti mare basalt. *Lunar Planet. Sci. Conf. Proc.* **9**, 705–724.

Jolliff B. L. (1991) Fragments of quartz monzodiorite and felsite in Apollo 14 soil particles. *Lunar Planet. Sci. Proc.* **21**, 101–118.

Jolliff B. L., Floss C., McCallum I. S. and Schwartz J. M. (1999) Geochemistry, petrology, and cooling history of 14161,7373: a plutonic lunar sample with textural evidence of granitic-fraction separation by silicate-liquid immiscibility. *Am. Mineral.* **84**, 821–837.

Jolliff B. L., Hughes J. M., Freeman J. J. and Zeigler R. A. (2006) Crystal chemistry of lunar merrillite and comparison to other meteoritic and planetary suites of whitlockite and merrillite. *Am. Mineral.* **91**, 1583–1595.

Kramers J. D., Gnos E., Hofmann B. A., Al-Kathiri A., Krause J., Brügmann G. E. and Pushkarev E. V. (2007) A ~4.3 Ga U–Pb age from lunar meteorite SaU169 and the chondritic Sm/Nd of the Moon. In *Goldschmidt Conference*, A520.

Li Q. L., Li X. H., Liu Y., Tang G. Q., Yang J. H. and Zhu W. G. (2010) Precise U–Pb and Pb–Pb dating of Phanerozoic baddeleyite by SIMS with oxygen flooding technique. *J. Anal. At. Spectrom.* **25**, 1107–1113.

Li X. H., Liu Y., Li Q. L., Guo C. H. and Chamberlain K. R. (2009) Precise determination of Phanerozoic zircon Pb/Pb age by multicollector SIMS without external standardization. *Geochem. Geophys. Geosyst.* **10**, Q04010.

Lin Y., Shen W., Liu Y., Xu L., Hofmann B. A., Mao Q., Tang G., Wu F. and Li X. (2010) Very high-K KREEP-rich clasts in the impact melt breccia of the lunar meteorite SaU 169 – possible pristine urKREEP sample. *Meteorit. Planet. Sci.* **45**, #5114 (abstr.).

Liu D., Wan Y., Zhang Y., Dong C., Jolliff B. L., Zeigler R. A. and Korotev R. L. (2009) Age of zircons in the impact-melt breccia in SaU 169 lunar meteorite: Beijing SHRIMP II study. *Lunar Planet. Sci. Conf.* **40**, #2499 (abstr.).

Liu D., Jolliff B. L., Zeigler R. A., Wan Y., Zhang Y., Dong C. and Korotev R. L. (2010) A 3.91 billion year age for Apollo 12 high-thorium impact-melt breccias: products of Imbrium, or an older impact basin in the Procellarum KREEP terrane? *Lunar Planet. Sci. Conf.* **41**, #2477 (abstr.).

Marvin U. B., Lindstrom M. M., Holmberg B. B. and Martinez R. R. (1991) New observations on the quartz monzodiorite–granite suite. *Lunar Planet. Sci. Proc.* **21**, 119–135.

Meldrum A., Boatner L. A., Weber W. J. and Ewing R. C. (1998) Radiation damage in zircon and monazite. *Geochim. Cosmochim. Acta* **62**, 2509–2520.

Meyer J., Elkins-Tanton L. and Wisdom J. (2010) Coupled thermal–orbital evolution of the early Moon. *Icarus* **208**, 1–10.

Neal C. R. and Taylor L. A. (1988) The splitting of KREEP into identifiable components: the "K-Frac" and "REEP-Frac" hypothesis. In *Workshop on Moon in Transition: Apollo 14, KREEP, and Evolved Lunar Rocks*, pp. 94–99.

Neal C. R. and Taylor L. A. (1989) Metasomatic products of the lunar magma ocean: the role of KREEP dissemination. *Geochim. Cosmochim. Acta* **53**, 529–541.

Neal C. R., Taylor L. A. and Patchen A. D. (1989a) High alumina (HA) and very high potassium (VHK) basalt clasts from Apollo 14 breccias: I. Mineralogy and petrology – evidence of crystallization from evolving magmas. *Lunar Planet. Sci. Conf. Proc.* **19**, 137–145.

Neal C. R., Taylor L. A., Schmitt R. A., Hughes S. S. and Lindstrom M. M. (1989b) High alumina (HA) and very high potassium (VHK) basalt clasts from Apollo 14 breccias: II. Whole rock geochemistry – further evidence for combined assimilation and fractional crystallization within the lunar crust. *Lunar Planet. Sci. Conf. Proc.* **19**, 147–161.

Nemchin A. A., Pidgeon R. T., Whitehouse M. J., Vaughan J. P. and Meyer C. (2008) SIMS U–Pb study of zircon from Apollo 14 and 17 breccias: implications for the evolution of lunar KREEP. *Geochim. Cosmochim. Acta* **72**, 668–689.

Ono S., Funakoshi K., Nakajima Y., Tange Y. and Katsura T. (2004) Phase transition of zircon at high *P–T* conditions. *Contrib. Mineral. Petrol.* **147**, 505–509.

Pidgeon R. T., Nemchin A. A. and Kamo S. L. (2011) Comparison of structures in zircons from lunar and terrestrial impactites. *Can. J. Earth Sci.* **48**, 107–116.

Pidgeon R. T., Nemchin A. A., van Bronswijk W., Geisler T., Meyer C., Compston W. and Williams I. S. (2007) Complex history of a zircon aggregate from lunar breccia 73235. *Geochim. Cosmochim. Acta* **71**, 1370–1381.

Rutherford M. J., Tonks B. and Holmberg B. (1996) Experimental study of KREEP basalt evolution: the origin of QMD and granite at the base of the lunar crust. *Lunar Planet. Sci. Conf.* **27**, 1113.

Ryder G., Stoeser D. B., Marvin U. B. and Bower J. F. (1975) Lunar granites with unique ternary feldspars. *Lunar Sci. Conf. Proc.* **6**, 435–449.

Seddio S. M., Korotev R. L., Jolliff B. L. and Zeigler R. A. (2010) Comparing the bulk compositions of lunar granites, with petrologic implications. *Lunar Planet. Sci. Conf.* **41**, #2688 (abstr.).

Shervais J. W., Taylor L. A., Laul J., Shih C. Y. and Nyquist L. (1985) Very high potassium (VHK) basalt: complications in mare basalt petrogenesis. *J. Geophys. Res.* **90**.

Snyder G. A., Taylor L. A. and Crozaz G. (1991) K-Frac and REEP-Frac immiscible liquids at Apollo 14: a SIMS search for the real urKREEP composition. *Lunar Planet. Sci. Conf.* **22**, 1291–1292 (abstr.).

Tange Y. and Takahashi E. (2004) Stability of the high-pressure polymorph of zircon ($ZrSiO_4$) in the deep mantle. *Phys. Earth Planet. Inter.* **143–144**, 223–229.

Warren P. H. (1988) The origin of pristine KREEP – effects of mixing between UrKREEP and the magmas parental to the Mg-rich cumulates. *Lunar Planet. Sci. Conf. Proc.* **18**, 233–241.

Warren P. H. and Wasson J. T. (1979) The origin of KREEP. *Rev. Geophys. Space Phys.* **17**, 73–88.

Warren P. H., Shirley D. N. and Kallemeyn G. W. (1986) A potpourri of pristine moon rocks, including a VHK mare basalt and a unique, augite-rich Apollo 17 anorthosite. *Lunar Planet. Sci. Conf. Proc.* **16**, D319–D330.

Wittmann A., Kenkmann T., Schmitt R. T. and Stöffler D. (2006) Shock-metamorphosed zircon in terrestrial impact craters. *Meteorit. Planet. Sci.* **41**, 433–454.

Zeigler R., Carpenter P., Jolliff B. and Korotev R. (2008) Trace-element analyses in lunar meteorite Sayh al Uhaymir 169. *Microsc. Microanal.* **14**(Suppl. 2), 112–113.

Zeigler R. A., Korotev R. L. and Jolliff B. L. (2006) Geochemistry and petrography of high-Th, mafic impact-melt breccia from Apollo 12 and Sayh Al Uhaymir 169. *Lunar Planet. Sci. Conf.* **37**, #2366 (abstr.).

Associate editor: Christian Koeberl